Surveys in Geophysics manuscript No.
(will be inserted by the editor)

Microseismic full waveform modeling in anisotropic media with moment tensor implementation

Peidong Shi · Doug Angus · Andy Nowacki · Sanyi Yuan · Yanyan Wang

Received: date / Accepted: date

Abstract Seismic anisotropy which is common in shale and fractured rocks will cause travel-time and amplitude discrepancy in different propagation directions. For

Peidong Shi

School of Earth and Environment, University of Leeds, Leeds, UK

Tel.: +4407761833640

E-mail: eepsh@leeds.ac.uk

Doug Angus (✉)

ESG Solutions, Kingston, Canada

Tel.: +16135488287 ext. 270

E-mail: d.angus@leeds.ac.uk

Andy Nowacki

School of Earth and Environment, University of Leeds, Leeds, UK

Sanyi Yuan

College of Geophysics and Information Engineering, China University of Petroleum, Beijing, China

Yanyan Wang

Department of Earth Sciences, ETH Zurich, Zurich, Switzerland

microseismic monitoring which is often implemented in shale or fractured rocks, seismic anisotropy needs to be carefully accounted for in source location and mechanism determination. We have developed an efficient finite-difference full waveform modeling tool with an arbitrary moment tensor source. The modeling tool is suitable for simulating wave propagation in anisotropic media for microseismic monitoring. As both dislocation and non-double-couple source are often observed in microseismic monitoring, an arbitrary moment tensor source is implemented in our forward modeling tool. The increments of shear stress are equally distributed on the staggered-grid to implement an accurate and symmetric moment tensor source. Our modeling tool provides an efficient way to obtain the Green's function in anisotropic media, which is the key of anisotropic moment tensor inversion and source mechanism characterization in microseismic monitoring. In our research, wavefields in anisotropic media have been carefully simulated and analysed in both surface array and downhole array. The variation characteristics of travel-time and amplitude of direct P- and S-wave in vertical transverse isotropic media and horizontal transverse isotropic media are distinct, thus providing a feasible way to distinguish and identify the anisotropic type of the subsurface. Analysing the travel-times and amplitudes of the microseismic data is a feasible way to estimate the orientation and density of the induced cracks in hydraulic fracturing. Our anisotropic modeling tool can be used to generate and analyse microseismic full wavefield with full moment tensor source in anisotropic media, which can help promote the anisotropic interpretation and inversion of field data.

Keywords Microseismic · Forward modeling · Seismic anisotropy · Moment tensor

1 Introduction

Full waveform modeling (FWM) can help us understand elastic wave propagation in complex media and is widely used in reverse time migration, full waveform inversion and seismic source imaging (Baysal et al 1983; Boyd 2006; Virieux and Operto 2009; Xuan and Sava 2010; Yuan et al 2014). There are two ways to calculate the full waveform solution in an elastic media: analytical solutions and numerical simulation. Analytical solutions, such as Green's function in an infinite half-space medium (Aki and Richards 2002), are mostly used in simple models such as homogeneous or layered media. Numerical solutions, such as finite-difference method (Kelly et al 1976), finite-element method (Zienkiewicz et al 1977) and spectral element method (Tromp et al 2008), are more suitable for modeling wave phenomena in complex media, but are computationally more expensive. Among the FWM methods, the finite-difference (FD) approach is widely used because of its flexibility in modeling wave propagation in complex media and excellent computational efficiency (Alterman and Karal 1968; Zienkiewicz et al 1977; Saenger et al 2000; Moczo et al 2002, 2014; Robertsson et al 2015). With the increase in modeling scale and complexity, a variety of ways have been proposed to improve the computational efficiency and modeling accuracy of the FD approach (Bohlen 2002; Michéa and Komatitsch 2010; Zhang and Yao 2013; Yao et al 2016).

In microseismic monitoring, FWM has been used as a reverse time modeling tool to locate the microseismic source using full waveform data (Gajewski and Tessmer 2005; Steiner et al 2008; Artman et al 2010; O'Brien et al 2011; Saenger et al 2011; Nakata and Beroza 2016). This method does not depend on arrival-time picking, therefore can be used on data with low signal-to-noise ratio. FWM is also used as a tool to generate and analyse the often complex full wavefield of microseismic data (Brzak et al 2009; Jin et al 2013; Li et al 2015), and to help improve the quality of microseismic imaging. The Green's function of the subsurface can be obtained through FWM, which is critical for the characterization of source mechanisms (Vavryčuk 2007; Kawakatsu and Montagner 2008; Song and Toksöz 2011; Li et al 2011; Chambers et al 2014; Linzer et al 2015). However, high frequency contents and accuracy requirement in microseismic monitoring have placed stringent demands on FWM (Hobro et al 2016). Compared with seismic data in conventional reflection seismology and global seismology, microseismic data have relatively high dominant frequency, which can have a significant influence on the character of the wavefield and waveforms (Usher et al 2013; Angus et al 2014). For downhole arrays which are deployed near microseismic events, the dominant frequency of microseismic signals can be a few hundred hertz. In order to obtain a reliable source mechanism characterization and comprehensive description of full wavefield, FWM with high-precision both in space and time domain is required for microseismic monitoring.

The moment tensor has been widely used to describe the source mechanisms of earthquakes (Aki and Richards 2002; Jost and Herrmann 1989). In natural and induced earthquakes (e.g. microseismicity), both double-couple and non-double-couple sources are observed. Earthquakes in volcanic, landslide and geothermal areas often have strong non-double-couple mechanisms (Miller et al 1998; Julian et al 1998). For induced earthquakes such as microseismicity due to hydraulic fracturing and mining, predominant non-double-couple source mechanisms are often observed (Foulger et al

2004; Šílenỳ and Milev 2008; Šílenỳ et al 2009). The induced non-double-couple events may result from opening cracks by high-pressure fluid injection (Šílenỳ et al 2009). Full moment tensor inversion is an efficient way to characterize the source mechanisms of microseismic events. Cesca et al (2013) used the full moment tensor inversion and decomposition to discriminate natural and induced seismicity. Modeling different types of sources and obtaining highly accurate Green's function is the key to perform full moment tensor inversion. Thus arbitrary moment tensor source representation in FWM is needed to fully describe the source mechanism of microseismic events.

Strong seismic anisotropy is often observed in shale and reservoirs which contain lots of natural and/or induced fractures (Johnston and Christensen 1995; Schoenberg and Sayers 1995; Vernik and Liu 1997; Wang 2002; Wang et al 2007; Yan et al 2016). Seismic anisotropy can have a significant influence on the recorded wavefields (both in travel-time and amplitude), and therefore increases the difficulty of microseismic data interpretation and inversion (Warpinski et al 2009). Both source location and mechanism inversion will be biased if seismic anisotropy is not incorporated or properly processed. The location error induced by seismic anisotropy is also related to the recording geometries of microseismic monitoring (Warpinski et al 2009). Rössler et al (2004) and Vavryčuk (2005) demonstrated that moment tensors for pure-shear sources will generally exhibit significant non-double-couple components in anisotropic media. Their studies show anisotropy can have a significant influence on the interpretation of the source mechanisms. Stierle et al (2016) demonstrated that the retrieve of moment tensor and source mechanism critically depend on anisotropy using laboratory acoustic emission experiments. Their study also shows that the tensile events are more sensitive to P-wave anisotropy than shear events. For source mechanism characterization, the P- and T-axes of the moment tensors are affected by velocity anisotropy and deviated form the true orientation of faulting (Stierle et al 2016). Understanding and correcting for wave propagation phenomena in anisotropic media will help to reduce uncertainties in source location and mechanism inversion. Grechka and Yaskevich (2013a) demonstrated that the travel-times of microseismic events can provide sufficient information to constrain both locations of microseismic events and the underlying anisotropic velocity model. They use the shear-wave splitting to improve the precision of event locations and locate events whose P-wave time picks are unavailable. A correct analysis of the source mechanism is also achievable through anisotropic moment tensor inversion (Rössler et al 2004). Seismic anisotropy can be retrieved from the recorded microseismic data (Al-Harrasi et al 2011; Zhang et al 2013). For a reliable estimation of seismic anisotropy, a wide aperture of recording array is normally required (Grechka and Yaskevich 2013b). Furthermore seismic anisotropy attributes can also provide more information about the fractured media and for seismic source inversion. Hydraulic fracturing can cause time-lapse changes in the anisotropy parameters. Grechka et al (2011) found the time-lapse changes in the anisotropy parameters rather than velocity heterogeneity need to be introduced to explain the microseismic data recorded at different fracturing stage. The time-lapse changes in the anisotropy parameters can be used to characterize the stimulated reservoir volume or crustal stress variation in cracked rock (Teanby et al 2004). The crack properties such as orientation and density can be studied using seismic anisotropy

(Verdon et al 2009; Wuestefeld et al 2010). Therefore anisotropic FWM is required in order to investigate the induced fracture properties and conduct accurate microseismic source inversion in anisotropic media.

In exploration seismology, FWM with explosive source is widely used because seismic waves are often excited by explosives (Sheriff and Geldart 1995). In addition, anisotropic effect is often ignored in order to accelerate the computation of FWM. As seismic anisotropy and moment tensor source are important for microseismic monitoring, we developed an efficient FWM tool based on FD method, which is suitable for anisotropic media and arbitrary moment tensors. First, we describe the elastodynamic equations in anisotropic media and the special way to implement an accurate and symmetrical moment tensor source in the staggered grid. Then we compared the modeling results of a general non-double-couple moment tensor source with analytical solutions in homogeneous medium to confirm the correctness of this method. Because the far-field approximations are often used in microseismic monitoring, the magnitude of near-field components and far-field components are also compared and discussed in detail in the paper. In the modeling examples part, the wave propagation phenomena are simulated and discussed in both anisotropic layered model and 3-dimensional (3D) anisotropic overthrust model. And the influence of seismic anisotropy on microseismic data are simulated and analysed in detail both for surface and downhole arrays. We examine the feasibility of utilizing recorded microseismic data to estimate seismic anisotropy of the subsurface.

2 Theory

In this section, we present the elastodynamic equations in velocity-stress formation, moment-tensor source representation for the wavefield excitation and the numerical implementation of the elastodynamic equations.

2.1 Elastic wave equation in inhomogeneous and anisotropic media

In 3D Cartesian coordinate system, the equations of momentum conservation are given by

$$
\begin{aligned}
\rho \frac{\partial v_x}{\partial t} &= \frac{\partial \tau_{xx}}{\partial x} + \frac{\partial \tau_{xy}}{\partial y} + \frac{\partial \tau_{xz}}{\partial z}, \\
\rho \frac{\partial v_y}{\partial t} &= \frac{\partial \tau_{xy}}{\partial x} + \frac{\partial \tau_{yy}}{\partial y} + \frac{\partial \tau_{yz}}{\partial z}, \\
\rho \frac{\partial v_z}{\partial t} &= \frac{\partial \tau_{xz}}{\partial x} + \frac{\partial \tau_{yz}}{\partial y} + \frac{\partial \tau_{zz}}{\partial z}.
\end{aligned} \tag{1}
$$

After some transformation, the stress-strain relations can be expressed as

$$
\begin{aligned}
\frac{\partial \tau_{xx}}{\partial t} &= c_{11}\frac{\partial v_x}{\partial x} + c_{12}\frac{\partial v_y}{\partial y} + c_{13}\frac{\partial v_z}{\partial z} + c_{14}\left(\frac{\partial v_y}{\partial z} + \frac{\partial v_z}{\partial y}\right) \\
&\quad + c_{15}\left(\frac{\partial v_x}{\partial z} + \frac{\partial v_z}{\partial x}\right) + c_{16}\left(\frac{\partial v_x}{\partial y} + \frac{\partial v_y}{\partial x}\right), \\
\frac{\partial \tau_{yy}}{\partial t} &= c_{21}\frac{\partial v_x}{\partial x} + c_{22}\frac{\partial v_y}{\partial y} + c_{23}\frac{\partial v_z}{\partial z} + c_{24}\left(\frac{\partial v_y}{\partial z} + \frac{\partial v_z}{\partial y}\right) \\
&\quad + c_{25}\left(\frac{\partial v_x}{\partial z} + \frac{\partial v_z}{\partial x}\right) + c_{26}\left(\frac{\partial v_x}{\partial y} + \frac{\partial v_y}{\partial x}\right), \\
\frac{\partial \tau_{zz}}{\partial t} &= c_{31}\frac{\partial v_x}{\partial x} + c_{32}\frac{\partial v_y}{\partial y} + c_{33}\frac{\partial v_z}{\partial z} + c_{34}\left(\frac{\partial v_y}{\partial z} + \frac{\partial v_z}{\partial y}\right) \\
&\quad + c_{35}\left(\frac{\partial v_x}{\partial z} + \frac{\partial v_z}{\partial x}\right) + c_{36}\left(\frac{\partial v_x}{\partial y} + \frac{\partial v_y}{\partial x}\right), \\
\frac{\partial \tau_{yz}}{\partial t} &= c_{41}\frac{\partial v_x}{\partial x} + c_{42}\frac{\partial v_y}{\partial y} + c_{43}\frac{\partial v_z}{\partial z} + c_{44}\left(\frac{\partial v_y}{\partial z} + \frac{\partial v_z}{\partial y}\right) \\
&\quad + c_{45}\left(\frac{\partial v_x}{\partial z} + \frac{\partial v_z}{\partial x}\right) + c_{46}\left(\frac{\partial v_x}{\partial y} + \frac{\partial v_y}{\partial x}\right), \\
\frac{\partial \tau_{xz}}{\partial t} &= c_{51}\frac{\partial v_x}{\partial x} + c_{52}\frac{\partial v_y}{\partial y} + c_{53}\frac{\partial v_z}{\partial z} + c_{54}\left(\frac{\partial v_y}{\partial z} + \frac{\partial v_z}{\partial y}\right) \\
&\quad + c_{55}\left(\frac{\partial v_x}{\partial z} + \frac{\partial v_z}{\partial x}\right) + c_{56}\left(\frac{\partial v_x}{\partial y} + \frac{\partial v_y}{\partial x}\right), \\
\frac{\partial \tau_{xy}}{\partial t} &= c_{61}\frac{\partial v_x}{\partial x} + c_{62}\frac{\partial v_y}{\partial y} + c_{63}\frac{\partial v_z}{\partial z} + c_{64}\left(\frac{\partial v_y}{\partial z} + \frac{\partial v_z}{\partial y}\right) \\
&\quad + c_{65}\left(\frac{\partial v_x}{\partial z} + \frac{\partial v_z}{\partial x}\right) + c_{66}\left(\frac{\partial v_x}{\partial y} + \frac{\partial v_y}{\partial x}\right).
\end{aligned}
\tag{2}
$$

In these equations, (v_x, v_y, v_z) represent the particle velocity components along x-, y- and z-directions respectively and $(\tau_{xx}, \tau_{yy}, \tau_{zz}, \tau_{yz}, \tau_{xz}, \tau_{xy})$ are the components of the stress tensor. The medium is characterized by the elastic tensor c_{IJ} and density ρ. Here the fourth-order elastic tensor c_{ijkl} is expressed in Voigt notation (c_{IJ}). Because of symmetry, the elastic tensor has only 21 independent parameters in a general anisotropic medium, which describe a minimally symmetrical, triclinic system (Sheriff and Geldart 1995; Nowacki et al 2011). However the number of independent parameters can be further reduced if the symmetry system of the medium is higher than that of a generally anisotropic medium. For an isotropic medium which is commonly used in seismic modeling and has the highest symmetry system, there are only 2 independent elastic parameters. For vertical transverse isotropic (VTI) and horizontal transverse isotropic (HTI) medium, there are 5 independent elastic parameters (Thomsen 1986; Rüger 1997). For tilted transverse isotropic (TTI) medium, there are 7 independent elastic parameters (Montagner 1998). For orthorhombic medium, there are 9 independent elastic parameters (Tsvankin 1997). For monoclinic medium, there are 13 independent elastic parameters (Sayers 1998). When modeling in a medium with a lower symmetry system, the memory cost will increase greatly. Table 1 shows the comparison of memory costs in different symmetry systems. In a specific medium whose symmetry system is higher than or equal to that of orthorhombic media (e.g. orthorhombic, HTI, VTI and isotropic media), the elastic tensor has the same null components. Thus the stress-strain relations can be further simplified as

$$
\begin{aligned}
\frac{\partial \tau_{xx}}{\partial t} &= c_{11}\frac{\partial v_x}{\partial x} + c_{12}\frac{\partial v_y}{\partial y} + c_{13}\frac{\partial v_z}{\partial z},\\
\frac{\partial \tau_{yy}}{\partial t} &= c_{21}\frac{\partial v_x}{\partial x} + c_{22}\frac{\partial v_y}{\partial y} + c_{23}\frac{\partial v_z}{\partial z},\\
\frac{\partial \tau_{zz}}{\partial t} &= c_{31}\frac{\partial v_x}{\partial x} + c_{32}\frac{\partial v_y}{\partial y} + c_{33}\frac{\partial v_z}{\partial z},\\
\frac{\partial \tau_{yz}}{\partial t} &= c_{44}\left(\frac{\partial v_y}{\partial z} + \frac{\partial v_z}{\partial y}\right),\\
\frac{\partial \tau_{xz}}{\partial t} &= c_{55}\left(\frac{\partial v_x}{\partial z} + \frac{\partial v_z}{\partial x}\right),\\
\frac{\partial \tau_{xy}}{\partial t} &= c_{66}\left(\frac{\partial v_x}{\partial y} + \frac{\partial v_y}{\partial x}\right).
\end{aligned}
\tag{3}
$$

Finally equations (1) together with equations (3) form the basic elastodynamic equations which can be used to simulate elastic wave propagation in orthorhombic, HTI, VTI and isotropic media. For HTI and VTI media, the elastic parameters can be characterized by elastic parameters of the corresponding isotropic medium in combination with Thomsen anisotropic parameters (Thomsen 1986). If the anisotropic zone of the model is simple such as layered or blocky VTI or HTI media, our FD modeling algorithm will first set up indexes which can represent the anisotropy of the model before modeling and obtain the elastic parameters from isotropic elastic parameters and Thomsen anisotropic parameters in the process of simulation. In this way, we can reduce the memory cost of HTI and VTI media to the same level of isotropic media.

2.2 Numerical implementation

The standard staggered-grid FD method (Virieux 1984, 1986; Dong and McMechan 1995) is employed to solve the elastodynamic equations of velocity-stress formation. In the standard staggered-grid method, wavefield components are discretized and distributed on different numerical grids both in time and space directions in order to solve the wavefield derivatives using central difference at the corresponding grid locations. The standard staggered-grid method is especially suitable and efficient for handling orthorhombic, HTI, VTI and isotropic medium. When modeling in these media using the standard staggered-grid method, no interpolation is necessary. Thus it is computationally fast and of low memory cost compared to the rotated-staggered grid method (Saenger et al 2000) or Lebedev scheme (Lisitsa and Vishnevskiy 2010; Xu 2012). Figure 1 shows the discrete standard staggered-grid used in the FD modeling. The wavefield components and medium elastic parameters are distributed on seven different staggered grids.

The spatial and temporal derivatives of the wavefield components in elastodynamic equations (1) and (3) are calculated through

$$\frac{\partial f}{\partial x} = \frac{1}{\Delta x} \sum_{n=1}^{L} c_n \left[f(x + n\Delta x - 0.5\Delta x) - f(x - n\Delta x + 0.5\Delta x) \right], \tag{4}$$

where c_n represents FD coefficients and $2L$ is the order of the FD scheme. For FD modeling, serious numerical artifacts will arise in the presence of high-frequency wavefield-components or coarse grids (Zhang and Yao 2013). Different than global or regional earthquake data, high frequency components of the recorded signals are often observed in microseismic monitoring. For microseismic applications, amplitude fidelity and azimuthal variations of signals are critical to microseismic processing and interpretation. Thus an accurate FD scheme is required for microseismic full-waveform modeling. Through equation 4, an FD scheme of arbitrary order can be easily achieved. High order FD schemes can ensure high modeling accuracy, but bring extra computational and memory cost. In practice, a balance between modeling accuracy and computational cost is needed. For FWM in anisotropic media, the wavefield complexity caused by seismic anisotropy is sometimes subtle. The relative wavefield difference compared to the isotropic scenario may be just a few percent. In addition, due to the influence of source radiation pattern, near-field effects also need to be considered (detailed discussion can be found in Appendix C). Therefore, a high order FD scheme is necessary. A FD scheme of 10th-order in space domain and 2nd-order in time domain is employed in our FWM, which provides sufficient accuracy requirement of anisotropic modeling with arbitrary moment tensor. There are many optimized schemes of FD methods which try to increase modeling accuracy and reduce numerical dispersion (Holberg 1987; Lele 1992; Liu and Sen 2009).

Optimized FD coefficients are adopted in this standard staggered-grid FD modeling scheme according to Holberg (1987).

Before starting forward modeling, the spatial interval Δh (constant in three directions here) of the grid need to be determined by fulfilling the grid dispersion criterion $\Delta h \leq v_{min}/(2nf_m)$, where v_{min} is the minimal S-wave velocity of the model, f_m is the peak frequency of the source time function and n is the number of grid-points per wavelength. If 10th order and Holberg type of FD operators are used in the modeling, n is 3.19. For a stable numerical modeling, the temporal interval Δt must satisfy the Courant-Friedrichs-Lewy criterion $\Delta t \leq \Delta h/(\sqrt{3}mv_{max})$, where v_{max} is the maximum P-wave velocity of the model and m is a factor which depends on the order and type of the FD operator. If 10th order and Holberg type of FD operators are used in the modeling, m is 1.38766.

2.3 Modeling efficiency and memory cost

The spatial interval of the grid (Δh) and temporal interval (Δt) are constrained by the dominant frequency (f_m) of the source time function. If high frequency is used in the modeling (which is often the case in microseismic modeling), the spatial and temporal intervals need to be reduced to make the modeling stable. Thus the simulation time will increase greatly. Our FWM tool is parallelized based on a shared memory architecture using OpenMP. In order to examine the parallel performance, we conducted anisotropic full waveform simulations of 10 time steps on different grid sizes and number of computer cores. The simulation time is illustrated in Table 2. Based on

Table 2, we can analyze the speedup ratio and parallel performance of our anisotropic FWM tool.

Figure 2(a) shows the speedup ratios of different model sizes. The dark dashed line exhibits the theoretical speedup ratio. We can see the model size of $600\times600\times600$ shows the best speedup ratio. Under the model size of $600 \times 600 \times 600$, the speedup ratio increases with the model size. In our parallel FD modeling algorithm, the computational workload is not equally allocated on all the available computational cores or threads at the beginning of parallel computing (static scheduling scheme). In order to distribute the workload more wisely and dispatch the calculation more efficiently, we adopt dynamic scheduling scheme of the workload. During parallel computing, each computational core/thread will be immediately assigned a new job after finishing the former assigned job. After testing, we find the dynamic scheduling scheme can achieve much better computational efficiency than the static scheduling scheme. However, when the modeling size is very large, the overhead computational cost due to the handling and distributing of the workload dynamically may hinder the parallel computing efficiency. As presented in Figure 2(a), the speedup ratios vary with different model sizes, and are all satisfactory for large model sizes (except $100\times100\times100$). The subtle difference of speedup performance on large model size may be due to the dynamic allocation of the workload on computational cores. Figure 2(b) shows the variation of simulation times with different grid sizes. The simulation time increases linearly with the grid size, which demonstrates our FWM tool scales well.

For microseismic modeling, high dominant frequency components are often needed. This will involve long simulation time and huge memory cost. If the dominant frequency of source time function is increased by n times ($f_m \rightarrow nf_m$), the spatial and temporal intervals will need to be reduced by n times. Thus in 3 dimensions, the calculation will increase by n^4 times under ideal conditions. Table 3 compares the modeling parameters and requirements under different frequencies. Here we assume the maximum P-wave velocity is 6000 m/s, the minimal S-wave velocity is 2000 m/s, the length of the simulation area is 3 km in each direction and the simulation time is 4 second (which is a common parameter settings for microseismic modeling). The CPU times (hour/CPU) are estimated using the simulation time of 10 time steps for model size $100 \times 100 \times 100$ and 1 core (1.730469 s in Table 2). Here we assume the computational complexity increases linearly with the grid size. Memory costs are estimated based on single precision. When parallel computing is applied, the calculation burden and memory cost are still acceptable for dominant frequency up to 150 Hz.

2.4 Moment tensor source implementation in staggered-grid

Two kinds of wavefield excitation conditions are commonly used in full-waveform FD modeling. One is the use of body-force term which acts on equations of momentum conservation (Aboudi 1971; Kosloff et al 1989; Yomogida and Etgen 1993; Graves 1996). The other one is to add an incremental stress on stress components (Virieux 1986; Coutant et al 1995; Pitarka 1999; Narayan 2001; Li et al 2014). Compared with the direct use of body-force term, the implementation of incremental stress in FD scheme is more straightforward. In this paper, the incremental stress method is adopted in order to implement an arbitrary moment tensor source into the FWM scheme.

Seismic moment tensor can be expressed as

$$\mathbf{M} = M_0 \cdot \mathbf{m} \cdot S(t), \tag{5}$$

where M_0 is the seismic moment, $\mathbf{m}$ contains nine moment tensor components m_{ij} and $S(t)$ is the source time function. The scalar seismic moment could be expressed as $M_0 = \mu AD$, where μ is shear modulus of the rocks involved in the source area, A is the area of the rupture and D is the average displacement during rupture. The seismic moment M_0 has the same units of energy and is often used to estimate the moment magnitude scale of an earthquake. $\mathbf{m}$ is symmetric and normalized such that $\sum_{ij} m_{ij}^2 = 1$.

Normally the incremental normal and shear stresses are applied directly on the corresponding grid points. However, in the staggered-grid FD approach, the normal stresses and shear stresses are not evaluated at the same position. Thus, simply applying incremental stresses directly on the stress components of the corresponding grid points as the conventional modeling methods do (Pitarka 1999; Narayan 2001; Li et al 2014) will not result in an exact moment tensor source. When implementing the moment tensor source in our staggered-grid FWM, in order to obtain a symmetrical moment tensor solution, we interpolate incremental shear-stress on four adjacent shear-stress grid points. Assuming a moment tensor point source acting at the grid position of the normal stress components, the location of the normal stress components will act as a central point. In order to obtain a symmetric moment tensor source, we evenly distribute the shear stress increments on the four adjacent shear stress grid points around the true moment tensor source location. Thus in total, there are twelve adjacent grid points around the true location of the moment tensor point source, which are numerically implemented with shear stress components (as shown by the blue grid points in Figure 1). The complete formulation for a moment tensor point source acting at the staggered-grid node i,j,k (i.e. the grid position of the normal stress components) is given by

$$
\begin{aligned}
\tau_{xx}(i,j,k) &= \tau_{xx}(i,j,k) - \frac{\Delta t}{V}\frac{\partial M_{xx}(t)}{\partial t},\\
\tau_{yy}(i,j,k) &= \tau_{yy}(i,j,k) - \frac{\Delta t}{V}\frac{\partial M_{yy}(t)}{\partial t},\\
\tau_{zz}(i,j,k) &= \tau_{zz}(i,j,k) - \frac{\Delta t}{V}\frac{\partial M_{zz}(t)}{\partial t},\\
\tau_{yz}(i,j+1/2,k+1/2) &= \tau_{yz}(i,j+1/2,k+1/2) - \frac{\Delta t}{4V}\frac{\partial M_{yz}(t)}{\partial t},\\
\tau_{yz}(i,j+1/2,k-1/2) &= \tau_{yz}(i,j+1/2,k-1/2) - \frac{\Delta t}{4V}\frac{\partial M_{yz}(t)}{\partial t},\\
\tau_{yz}(i,j-1/2,k+1/2) &= \tau_{yz}(i,j-1/2,k+1/2) - \frac{\Delta t}{4V}\frac{\partial M_{yz}(t)}{\partial t},\\
\tau_{yz}(i,j-1/2,k-1/2) &= \tau_{yz}(i,j-1/2,k-1/2) - \frac{\Delta t}{4V}\frac{\partial M_{yz}(t)}{\partial t},\\
\tau_{xz}(i+1/2,j,k+1/2) &= \tau_{xz}(i+1/2,j,k+1/2) - \frac{\Delta t}{4V}\frac{\partial M_{xz}(t)}{\partial t},\\
\tau_{xz}(i+1/2,j,k-1/2) &= \tau_{xz}(i+1/2,j,k-1/2) - \frac{\Delta t}{4V}\frac{\partial M_{xz}(t)}{\partial t},\\
\tau_{xz}(i-1/2,j,k+1/2) &= \tau_{xz}(i-1/2,j,k+1/2) - \frac{\Delta t}{4V}\frac{\partial M_{xz}(t)}{\partial t},\\
\tau_{xz}(i-1/2,j,k-1/2) &= \tau_{xz}(i-1/2,j,k-1/2) - \frac{\Delta t}{4V}\frac{\partial M_{xz}(t)}{\partial t},\\
\tau_{xy}(i+1/2,j+1/2,k) &= \tau_{xy}(i+1/2,j+1/2,k) - \frac{\Delta t}{4V}\frac{\partial M_{xy}(t)}{\partial t},\\
\tau_{xy}(i+1/2,j-1/2,k) &= \tau_{xy}(i+1/2,j-1/2,k) - \frac{\Delta t}{4V}\frac{\partial M_{xy}(t)}{\partial t},\\
\tau_{xy}(i-1/2,j+1/2,k) &= \tau_{xy}(i-1/2,j+1/2,k) - \frac{\Delta t}{4V}\frac{\partial M_{xy}(t)}{\partial t},\\
\tau_{xy}(i-1/2,j-1/2,k) &= \tau_{xy}(i-1/2,j-1/2,k) - \frac{\Delta t}{4V}\frac{\partial M_{xy}(t)}{\partial t},
\end{aligned}
\tag{6}
$$

where $V = \Delta x \cdot \Delta y \cdot \Delta z$ is the effective volume of the grid cell, and Δt is the time spacing of FD modeling. In the velocity-stress FD scheme (equation 1 and 2), the temporal derivative of the moment tensor is used, because the temporal derivatives of the stress components are used in the elastodynamic equations. However for moment tensor source implementation in the displacement-stress FD scheme, the moment tensor itself is used instead of its temporal derivative. And the time spacing item in these equations also disappears.

2.5 Validation with analytical solutions

For microseismic monitoring where high frequency data are often recorded, it is naturally favourable to consider only the far-field approximation. However, there are scenarios where the effect of near-field terms and intermediate-field terms can not be ignored (Vidale 1995). Full waveform FD modeling can provide a step improvement in accurately modeling all kinds of wave phenomena both in the near-field and far-field. We compare the synthetic displacement field in the Y direction using our FWM method with the analytical solutions (based on equation 15 in Appendix B). The elastic parameters of the medium used are $v_p = 3500\ m/s$, $v_s = 2000\ m/s$ and $\rho = 2400\ kg/m^3$. The source time function is a Ricker wavelet with a peak frequency of 40 Hz and a time delay of $1.1/f_m$ (this source time function is also used in the remaining examples). For generality, a non-double-couple moment tensor source is adopted in the simulation. The non-double-couple moment tensor is given by

$$\mathbf{m} = \begin{pmatrix} 0.4532 & 0.2789 & 0.1743 \\ 0.2789 & -0.5926 & 0.1046 \\ 0.1743 & 0.1046 & 0.4532 \end{pmatrix}. \tag{7}$$

This moment tensor comprises 11% isotropic (explosion), 45% double-couple and 44% compensated linear vector dipole components, and can well represent a general non-double-couple moment tensor. We choose this combination in order to jointly illustrate the effects of the major equivalent forces which are expected in microseismic settings. Figure 3 shows the far-field P-wave and S-wave radiation patterns of this non-double-couple moment tensor source. In Figure 3, the vectors exhibit the polarization direction of the P- and S-waves and the color and length of the vectors represent the polarization strength.

Figure 4 shows the simulated waveforms and modeling residuals. For the finite-difference simulation, the spatial and temporal interval are 5 m and 0.1 ms respectively. The source-receiver distances of the twelve receivers range from $0.5\lambda_s$ to $8\lambda_s$ with a 86.4° opening angle to account for both near-field and far-field scenarios (λ_s is the dominant S-wave wavelength, which is 50 m in this simulation experiment). The twelve receivers are deployed with azimuth angles varying from 0° to 85°. As shown in Figure 4(a), the waveform fidelity of the finite-difference results is in good agreement for both the near-field and far-field terms, with no obvious amplitude differences or phase shifts with respect to the analytical solution. This is also verified by Figure 4(b) which shows the relative error of the peak amplitude with respect to the analytical solution. The relative errors of the 10th- and 12th-order (in space domain)

FD scheme are within 1% both in the near-field and far-field. The relative errors of the 8th-order FD scheme are greater than 2% in the near-field. As the 10th-order FD scheme provides sufficient modeling accuracy, we will adopt 10th-order as the default FD scheme in the following modeling examples. However, the relative errors of the far-field approximation are much larger than that of the finite-difference method especially in the near-field. Considering the inevitable simulation error brought in by numerical discretization, the accuracy of this finite-difference simulation is sufficient. Therefore, the finite-difference modeling can provide full-wavefield information and more accurate results than the far-field approximation.

3 Modeling examples

3.1 Anisotropic Layered Model

The subsurface medium can range in complexity, both in terms of elastic heterogeneity and anisotropy. In order to inspect the influence of anisotropy on the wavefield from a microseismic event, a simple block velocity model with three layers is examined. The layered model is often used in microseismic interpretation and inversion. As shown in Figure 5 (a), a microseismic event is located in the middle of the model. Surface and downhole arrays are commonly used in microseismic monitoring. In the modeling experiment, both a surface array and a vertical downhole array are deployed to record the microseismic data. In order to comprehensively assess the influence of seismic anisotropy on traveltimes and amplitudes of microseismic data, a dense surface array with full azimuth coverage is deployed. The surface array has

90000 geophones deployed uniformly along the free surface at 10 m intervals. The vertical downhole array is located at a horizontal distance of 283 m and an azimuth of 135° relative to the microseismic source (i.e. the middle of the model). The downhole array has 500 geophones with intervals of 5 m. In the second layer, where the microseismic event is located, we examine three submodels having three different types of anisotropy. In the first submodel, no anisotropy is introduced, which implies an isotropic layered setting. In the second submodel, the second layer is set to be VTI, which is used to simulate shale having horizontal stratification. In the third submodel, the second layer is set to be HTI, which is used to simulate rock with vertical fractures. For all the submodels, a vertical strike-slip event is used to simulate the microseismic source, which means only m_{xy} and m_{yx} are non-zero in the seismic moment tensor. The elastic parameters of the isotropic layered model are shown in Table 4. The velocity model used in the modeling is a simplified representation of geological structure typically encountered by hydraulic fracturing projects in the Barnett shale in Texas (Wong et al 2011). The VTI medium in the second example has Thomsen parameters of $\varepsilon = 0.334$, $\gamma = 0.575$, $\delta = 0.73$, which is a measured anisotropy in clayshale (Thomsen 1986). The HTI medium in the third submodel is constructed by rotating the VTI medium of the second submodel anticlockwise along the Y-axis by 90°.

The P- and S-wave velocity anisotropy of the VTI and HTI media used in the second layer in the submodels are shown in Figure 6 (a-c) and Figure 6 (d-f), respectively. The relative variation for the P-, fast and slow S-wave velocity in the VTI medium are 29.2%, 46.6% and 28.4% respectively. The velocity anisotropy of the HTI medium can be easily obtained by rotation.

Figure 7 (a-c) shows horizontal wavefield slices of particle velocity in the Y direction for the three submodels, where the wavefield is recorded at the depth of microseismic source. Different types of waves can be identified in these wavefield slices. For Figure 7(a), the isotropic case, only the P- and S-wave are identified in the wavefield slice. In the VTI anisotropic example shown in Figure 7(b), S-wave splitting is clearly observed seen by the distinct fast S-wave (qS1-wave) and slow S-wave (qS2-wave) in the wavefield. As the second layer is transversely isotropic, the wavefront in the horizontal slice does not show anisotropic velocity variation in the different propagation directions. In the third example, where the second layer is HTI medium, a more complex wavefield is observed. Due to strong anisotropy, the wavefronts of the different types of waves show strong anisotropy in the different propagation directions, and wavefront triplication is also observed in the slice.

Figure 7 (d-f) shows vertical wavefield slices of the particle velocity in the Y direction for the three submodels, where the vertical slice bisects the same Y-position of the microseismic source. Due to the existence of layer boundaries in these vertical slices, reflected waves, transmitted waves and mode-converted waves (e.g., converted PS-waves and converted SP-waves) appear in the wavefield slices, thus making the wavefield more complicated. For the VTI submodel, the vertical wavefield slice is not located in the transversely isotropic plane, thus strong anisotropy can be observed in the shape of the wavefront (as shown in Figure 7(e)). For the HTI submodel, where the orientation of the HTI medium is oriented such that the transversely isotropic plane is parallel to the Y-axis, the vertical wavefield displays strong anisotropy in the wavefront (as shown in Figure 7(f)). The presence of seismic anisotropy has made the wavefield much more complex compared to the isotropic case, increasing the complexity of microseismic processing, such as event detection and travel-time picking.

Downhole array

The recorded seismograms for the downhole array are shown in Figure 8. The recorded seismograms are the particle velocity component in the Y direction. The direct P- and S-wave are automatically picked in the recorded wavefields. Compared with the seismograms in the isotropic case, the seismograms for the anisotropic submodels are much more complicated. Due to S-wave splitting, more mode-converted and multi-reflected waves appear in the recorded data, thus making microseismic event detection and arrival-time picking more difficult. When many microseismic events are triggered in the target area within a short time, the extra complexity and interference in the wavefield introduced by the medium anisotropy of the target area will make microseismic location difficult.

To further study the influence of anisotropy on microseismic monitoring, travel-times and peak amplitudes of the direct P-wave in the three submodels are extracted and compared. As Figure 9 shows, when the subsurface medium shows strong anisotropy, the amplitudes and travel-times of the direct P-wave will be variable. The maximum relative differences in travel-time and peak amplitude are 16% and 86% for the VTI case, and 18% and 50% for the HTI case. The travel-time and amplitude differences between the anisotropic models and the isotropic model are not constant, and vary with wave propagation direction due to anisotropy. The amplitude of the recorded waveforms is mainly affected by the radiation pattern of the source, coupling between different phases and the elastic properties of the media such as impedance and attenuation. Because of seismic anisotropy, wave velocity varies with different propagation directions. Thus the ray path and media elastic parameters in anisotropic cases are different from those in isotropic case. In this way, the seismic anisotropy has affected the travel-time and amplitude of the recorded waves and hence the observed radiation pattern of the microseismic source. Thus without considering seismic anisotropy, the variation in travel-time and amplitude in the different directions will bias the final result, thus contributing to large errors in inverted source location and mechanism. As shown in Figure 9(b), when geophones are located in the anisotropic layer, the travel-time difference of the direct P-wave in the VTI and HTI models with respect to the isotropic model exhibit opposing trends. For the VTI model, the travel-time difference increases with the take-off angle of the seismic rays, whereas for the HTI model, the travel-time difference decreases with the take-off angle of the seismic rays. The travel-time difference can be expressed by

$$\Delta t = \frac{l_{ref}}{v_{ref}} - \frac{l_{ani}}{v_{ani}}, \tag{8}$$

where l represents the ray path in the isotropic reference medium or anisotropic medium; v_{ref} is the average group velocity along the ray path in the reference medium (which is the P-wave velocity of the isotropic model here); v_{ani} is the average group velocity along the ray path in the anisotropic medium. The average group velocity of the reference medium v_{ref} will only affect the sign of the travel-time difference and not the trend of the travel-time difference. In practice, the reference velocity can be determined by well logging data, which is an approximation for the velocity in the vertical direction. Due to the simplicity of the adopted anisotropic model, the ray path in the isotropic and anisotropic media could be considered approximately the same, which is often the case in the near-field and for smooth velocity models (Sadri and Riahi 2010; Wang 2013). Thus the travel-time difference is proportional to the length of ray path and average group velocity of the anisotropic medium along the ray path. Under the current modeling geometry, the length of the ray path decreases with the take-off angle of the seismic rays. However, the downhole array is deployed near the source region and thus velocity variation of the anisotropic medium along different propagation directions is the main control factor for travel-time differences. When the recording array is deployed far enough away from the source region, such as surface arrays, the length of the ray path should be taken into consideration when analysing travel-time differences.

As we have shown, the different types of velocity anisotropy can cause different trends in travel-time differences. The distribution of phase velocities of P-wave, slow S-wave and fast S-wave in 3D space domain forms the velocity surface corresponding to these three phases (Babuska and Cara 1991). Figure 10 shows the velocity surfaces in the profile of the downhole array for the isotropic model, VTI model and HTI model. The P-wave velocity towards the directions of downhole geophones in the second layer are calculated and shown in Figure 11(b). For the VTI medium, the P-wave velocity increases with the take-off angle. However, for the HTI medium, the P-wave velocity decreases with the take-off angle at this particular azimuth. The normalized travel-time difference of the direct P-wave for the downhole geophones in the second layer is shown in Figure 11(c). Because the receivers are placed at the same layer, ray path can be easily calculated. In Figure 11(c), the effect of the ray path has been considered and eliminated, thus the travel-time differences are only influenced by the P-wave velocity. Figure 11(b) and 11(c) show strong similarity and potentially provides a way to estimate the anisotropy of the target zone in microseismic monitoring. As well, the VTI and HTI media can be distinguished using a downhole array. For the TTI media, the travel-time difference will not monotonically increase or decrease with the take-off angle as for the VTI and HTI media.

The variation in travel-times and peak-amplitudes for the fast S-wave (S-wave in isotropic case) in the different models are shown in Figure 12. In Figure 12(c), the peak amplitudes of the fast S-wave in the VTI model shows a big difference with that in the isotropic and HTI models. From the recorded waveform in Figure 13 (a-b), we can clearly see that seismic anisotropy has completely changed the radiation pattern of the S-wave in the VTI model.

The velocity difference or travel-time difference between the fast S-wave and the slow S-wave can be used to describe the shear-wave anisotropy in an anisotropic medium. Large velocity differences between fast and slow shear-waves will cause strong shear-wave splitting (i.e. splitting time). Shear-wave anisotropy is used to describe shear-wave splitting strength. It is defined as the ratio between the difference and average of fast and slow shear-waves ($aV_s = (V_{qS1} - V_{qS2})/0.5(V_{qS1} + V_{qS2})$) (Walker and Wookey 2012). Figure 13 (c-d) shows the variation of shear-wave anisotropy in the VTI and HTI models. The travel-time difference between the fast S-wave and the slow S-wave are also extracted and displayed in Figure 14(a).

The normalized travel-time difference after eliminating the influence of the ray-path (Figure 14(b)) shows good consistency with the velocity difference (Figure 14(c)) suggesting that this is a feasible way to estimate the anisotropy of the subsurface in microseismic monitoring. The recorded fast and slow S-waves in anisotropic media can be identified and studied through shear-wave splitting analysis (Crampin and Peacock 2008; Long and Silver 2009). We note that inversion of shear-wave splitting data for anisotropy and fracture parameters is increasingly common (Wuestefeld et al 2010; Verdon et al 2011). Our method enables the easy comparison of geomechanical models to the data by fully reproducing the wavefield in generally anisotropic media.

Surface array

Figure 15 shows seismic profiles along the first line in the Y direction of the surface array. The direct P-wave arrivals are automatically picked in the recorded wavefields. Four traces in Figure 15 are extracted and shown in Figure 16. Due to the strong seismic anisotropy, the received seismic waveforms for the VTI and HTI submodels are quite different compared to the isotropic case. More phases can be observed in the anisotropic models because of shear-wave splitting. If care is not taken, these phases could be identified as true microseismic events having detrimental effect on microseismic interpretation.

Figure 17 shows the travel-times of the direct P-wave along the free surface. As the surface array is deployed uniformly on the free surface and the microseismic source is located just below the middle of the surface array, the travel-times of the seismic waves in the isotropic layered media should be symmetrical about the epicenter, as can be seen in Figure 17(a), where the travel-times of the direct P-wave are circular. In the VTI model, the transverse isotropic symmetry plane is in the horizontal plane, and so the travel-times of the direct P-wave are also circular (Figure 17(b)). The magnitude of travel-time differs from the isotropic case due to the presence of anisotropy. However, in HTI model, the transverse isotropic symmetry plane is vertical, thus velocity anisotropy in the horizontal plane will contribute to an asymmetric distribution about the epicenter. As Figure 17(c) shows, travel-times of the direct P-wave are ellipses in the HTI model. The major axis of ellipse is parallel to the isotropic plane of the HTI medium, which is along the orientation of the fracture planes. The ratio of the major and minor axes of the ellipse is proportional to the strength of anisotropy. Travel-time differences of the direct P-wave between the anisotropic models and the isotropic model are shown in Figure 18, which clearly exhibits the different characteristics of VTI and HTI media and the alteration of travel-times introduced by seismic anisotropy.

Figure 19 shows the peak amplitudes and also the polarization of the direct P-wave. The maximum relative difference of peak amplitude can be as large as 50% for VTI and HTI, which means seismic anisotropy can have a large influence on source mechanism characterization, such as moment tensor inversion. As shown in Figure 19, the peak amplitudes of the direct P-wave in anisotropic case is smaller than that in isotropic case. This will cause an underestimate of the seismic moment M_0 in the presence of anisotropy when only direct P-waves are used in the source magnitude estimation. In Figure 19, the polarizations of the direct P-wave have not been significantly affected by seismic anisotropy. The peak amplitude differences of the direct P-wave between the anisotropic models and the isotropic model are also shown in Figure 20, which clearly shows the alteration of amplitudes introduced by seismic anisotropy.

Source location error due to seismic anisotropy

If seismic anisotropy is ignored in microseismic event location, the location result will be biased (King and Talebi 2007; Warpinski et al 2009). Table 5 compares the event location results in isotropic, VTI and HTI models using the recorded P-wave arrival times of the surface array. The microseismic event is located by minimising the overall difference between the recorded arrival times and the calculated theoretical traveltimes. The theoretical traveltimes of direct P-waves are calculated at every discretized grid points based on the accurate isotropic velocity model. The event location results in Table 5 show the influence of different types of anisotropy. In the isotropic model, the microseismic event has been located accurately. In VTI and HTI models, the located event is deeper than the correct event, with vertical deviations of 570 m and 190 m respectively. Here, because the surface array is symmetric about the hypocenter of the microseismic event, the located event is well constrained in the horizontal direction. Therefore, no location deviations in X or Y directions are observed.

The seismic anisotropy has changed the curvature of the direct arrivals (see figure 15 and 17), and therefore brings large errors for seismic location. The cumulative traveltime residual is used to evaluate the inversion error. It is defined as $\sqrt{\sum_i^N (t_i^a - t_i^c)^2}$, where t_i^a is the recorded arrival times, t_i^c is the calculated theoretical arrival times at the estimated event location and N is the number of receivers. The cumulative traveltime residual in the isotropic model should be 0. However, due to some inevitable picking errors of the direct P-waves, the cumulative traveltime residual in the isotropic model shows a very small value. In Table 5, the cumulative traveltime residual in the HTI model is much larger than that in VTI and isotropic models. This is because the arrival times of direct waves in the HTI model exhibit elliptical anisotropy for the surface array, which is different from the round distribution of arrival times in VTI and isotropic models (as shown in Figure 17). Therefore, the calculated arrival times cannot match the recorded arrival times very well. Due to the trade-off between location depth and estimated origin time of seismic event, when the located event is deeper, the estimated origin time of the event is earlier than the correct origin time (as can be seen in our location results in VTI and HTI models in Table 5). The location error in the VTI model is much larger than the HTI model, and the estimated origin time is also much earlier. In microseismic monitoring, a few hundred meters deviation of event location can be fatal for assessing the fracturing effect or microseismic mapping. Therefore, seismic anisotropy need to be accounted for in microseismic monitoring especially when large amount of fractures have been stimulated by fracturing.

3.2 Anisotropic Overthrust Model

Based on the previous simple models, it is not surprising that microseismic imaging in complex media is a challenge. In complex media, the influence of seismic anisotropy could be further distorted due to the presence of elastic heterogeneity.

In order to study the influence of seismic anisotropy on microseismic monitoring in complex media, we apply full waveform modeling in the 3D isotropic and anisotropic SEG/EAGE overthrust model (Aminzadeh et al 1997), which has been widely used in exploration geophysics (Virieux and Operto 2009; Yuan et al 2015). Three overthrust models with different types of anisotropy are used in the simulations. The P-wave velocity of the overthrust model is shown in Figure 21. The overthrust model has a size of $801 \times 801 \times 187$ cells in the X, Y and Z directions. The same double-couple source (vertical strike-slip) is placed in the middle of the 3D model, (i.e., grid coordinate 400, 400 and 93 in X, Y and Z directions). Around the source, an anisotropic region is set up (marked by the black lines in Figure 22). In the anisotropic region, different models are set to have different types of anisotropy, which are isotropy, VTI anisotropy and HTI anisotropy. The VTI anisotropy has the same Thomsen anisotropic parameters (i.e., $\varepsilon = 0.334$, $\gamma = 0.575$ and $\delta = 0.73$) as the former VTI modeling example. The HTI medium is constructed by rotating the VTI medium counter-clockwise along the Y-axis by 90°. Figure 22 shows three profiles of the overthrust model, in which the source location and anisotropic volume are clearly marked. As Figure 22 shows, the 3D SEG/EAGE overthrust model contains lots of faults (Figure 22(b) and 22(c)) and fluvial deposits (Figure 22(a)), which are suitable for studying the influence of anisotropy in complex heterogeneous media. Both a surface array (149×149 geophones at 25 m intervals) and a vertical downhole array (127 geophones at 5 m intervals) are used to record the microseismic data in the simulations.

Figure 23 shows the wavefield snapshots of these three modelings. Compared with the wavefield in the isotropic model, the wavefield in the anisotropic models is much more complex due to seismic anisotropy, especially in the anisotropic region. This complexity arises from the shear-wave splitting and velocity contrast between isotropic region and anisotropic region.

Figure 24 shows the recorded seismograms of the downhole array in different models. The strong heterogeneity has made the wavefields very complex, where abundant reflected and multiple waves can be seen in the recorded seismograms. In the presence of anisotropy, the model complexity has added to the general complexity of anisotropic phenomena. Significant differences of the recorded seismograms between the anisotropic models and the isotropic model can be seen in Figure 24.

The travel-times and peak amplitudes of the direct P-wave have been automatically picked and displayed in Figure 25. As with the previous analysis in the layered model, the travel-time differences of the direct P-wave in the VTI model increases with take-off angle of the rays and exhibits an upside down U shape pattern in the downhole array. On the contrary, the travel-time differences of the direct P-wave in the HTI model exhibits an opposite trend in the downhole array. The amplitudes of the direct P-waves are also different in the anisotropic scenarios. The maximum relative differences for travel-times and amplitudes are 17% and 80% respectively in the anisotropic models.

The seismic profiles recorded by surface array are shown in Figure 26. Significant differences in the recorded wavefields can be observed between the isotropic, VTI and HTI models. The direct P-waves recorded by the surface array are automatically picked. The picked travel-times and peak amplitudes of the direct P-wave are shown in Figures 27 and 28. Because of the complexity of the recorded wavefields and weak strength of the direct P-wave, the automatic picking is not perfect. Some picking errors can be seen in the figures and the picked peak amplitudes are blurred. However the radiation pattern of the direct P-wave can be recognised both in the isotropic and the VTI models. The radiation pattern of the direct P-wave in HTI model is affected by picking error and cannot be recognised easily. In this situation, the manual picking is required. The surface array is symmetrical about the epicenter of the source. The travel-times of the direct P-wave in VTI model maintain the circular distribution as in the isotropic model because the transverse isotropic symmetry plane is in the horizontal plane. However the travel-times of the direct P-wave in HTI model exhibit an ellipse distribution because of the anisotropy in the horizontal plane. The major axis of the ellipse is parallel to the direction of the isotropic plane of the HTI media, and the minor axis of the ellipse is parallel to the direction of the symmetry axis of the HTI media. And the ratio of the major axis to the minor axis is proportional to the strength of anisotropy. In reality, if a microseismic source is located, we can pick out the same phases with the same offset but at different azimuth angles in the surface array and compare the travel-time of these phases. As the dense surface array with wide-azimuth is increasingly used in the microseismic monitoring, it is not hard to find receivers which have the same offset but different azimuth angles. Thus in this way, we can estimated the orientation and density of the fractures using surface array in microseismic monitoring when the seismic anisotropy is caused by the vertical cracks induced by hydraulic fracturing. Through analysing anisotropy using surface array data of different events during hydraulic fracturing, we can also evaluate the fracturing effect and gain more knowledge about the fracturing process. Even through the ray path in different azimuth is different due to horizontal heterogeneity, the travel-time is not affected too much by the ray path. The influence of seismic anisotropy in travel-times is still observable and is more significant at relatively large offsets. This demonstrates it is feasible to estimate the seismic anisotropy of complex subsurface media using surface arrays. Seismic anisotropy obtained using surface array has been extensively used for fracture detection in exploration geophysics (Bakulin et al 2000; Wang et al 2007; Bachrach et al 2009). Effective anisotropy parameters and fracture characteristics can also be extracted from the microseismic surface monitoring (Wuestefeld et al 2010; Zhang et al 2013). The polarization of the direct P-wave is not seriously affected by anisotropy. However the variation in amplitude caused by anisotropy could introduce biases in moment tensor inversion.

4 Discussions and Conclusion

The primary focus of this study was to develop an efficient FD forward modeling tool with arbitrary moment tensor source, which can be used for simulating wave propagation phenomena in anisotropic media for microseismic monitoring. We have shown how to implement an symmetrical moment tensor source into the staggered-grid FD modeling scheme. We simulated and analysed the wavefields in both a 3D layered and a 3D overthrust anisotropic model using surface and downhole arrays. Because both VTI and HTI anisotropy are common in shale or fractured media, we focused only on wavefields in VTI, HTI and orthorhombic media.

Seismic anisotropy will make the recorded wavefield more complex and distort the amplitudes and arrival-times of the P- and S-waves, thus making microseismic imaging difficult. Retrieve seismic anisotropy from microseismic data is very helpful for characterizing the stimulated fracture properties in hydraulic fracturing. In practice, the effect of seismic anisotropy, source radiation pattern and geological structure on recorded wavefields may be difficult to separate. Therefore, trade-off among these effects may exist when analysing real microseismic data. In practice, the sensitivity and trade-off analysis should be performed on a case-by-case basis at each monitoring operation. An accurate velocity model is favourable for anisotropy analysis and moment tensor inversion. Many methods have been put forward to obtain highly accurate velocity model, such as full waveform inversion (Tarantola 2005), but on the basis of accurate forward modeling. The joint source location, mechanism determination and velocity inversion is also a promising way to obtain more practical solutions. By simultaneously using source location, mechanism and velocity information to minimise the misfit relative to recorded wavefields, better solution can be found with less trade-off among these properties. All these methods require the of anisotropic FWM we demonstrate here.

Most shale reservoirs in which hydraulic fracturing is often implemented have sub-horizontal bedding, where the beds also show sub-horizontal fabrics. Therefore, VTI can be a good approximation for this kind of anisotropy (Helbig and Thomsen 2005; Kendall et al 2007; Sone and Zoback 2013). Reflection seismic and borehole data can give a good control on the dips of beds, and also fracture orientations, which tend to be sub-vertical. Therefore, although we only simulate and analyse full wavefields in VTI and HTI media, both of these cases are often quite well constrained in practice. However, the combination of bedding/lattice-preferred-orientation (LPO) and fractures gives a lower symmetry to the anisotropy (orthorhombic), which can also be well simulated using our modeling tool. Apart from HTI, VTI and orthorhombic anisotropy, the subsurface can be more complex, such as TTI, monoclinic and general anisotropy. The wave propagation phenomena in these complex media will be more complicated. However, our FWM tool can be easily expanded to incorporate the general anisotropy, which can help promote the full anisotropic interpretation and inversion of field data. In addition, seismic anisotropy in combination with complex velocity heterogeneity will also make the interpretation and inversion of realistic data more difficult. Therefore, the full anisotropy interpretation and inversion of field data still need further development. Shear-wave splitting analysis (Crampin and Peacock 2008; Verdon et al 2009) is a powerful way to separate the shear-waves and provide anisotropic informations of the subsurface, such as fracture alignment, density and aspect-ratio.

Panza and Saraò (2000) pointed out that poor station coverage, mislocation of the hypocenter, noise and inadequate structural model can cause spurious non-double-couple mechanisms. When conducting real data analysis, error analysis based on synthetic full waveform tests must be performed to estimate the reliability of the source mechanism solutions. In addition, Vavryčuk (2004) proposed an inversion method to retrieve seismic anisotropy from non-double-couple components of seismic moment tensors. Unlike most anisotropy analysis methods which retrieve an overall anisotropy along a whole ray path, this inversion method can obtain the anisotropy just in the focal area. However, this inversion method requires obtaining highly accurate source moment tensor in anisotropic media. Therefore, it is necessary and important to develop an anisotropic modeling tool with arbitrary moment tensor source for testing, analyzing and benchmarking. Our FWM method provides an efficient modeling tool to generate and analyse the microseismic full wavefield with full moment tensor source in anisotropic media. The modeling feature in seismic anisotropy and arbitrary moment tensor source can help to conduct anisotropic full waveform inversion, anisotropy analysis and full moment tensor inversion.

In the complex overthrust model, when analysing travel-time differences, we did not eliminate the influence of ray path differences as we did in the layered model. However, the variation trends of travel-time differences with respect to take-off angle in VTI and HTI anisotropic scenarios are still established in the downhole array. And the variation of travel-time in the surface array also exhibit the same phenomenon as with in layered model. This is because the anisotropy is strong enough (as is often the case in shale or fracture-enriched layer) that the influence of velocity variation surmounts that of ray path differences in travel-time. However, when the variation of ray path is significant or the anisotropy is weak, the influence of ray path must be considered and eliminated in order to correctly evaluate the anisotropy. This will involve ray tracing in heterogeneous and/or anisotropic media.

Seismic anisotropy is an important property of shale rocks, where most hydraulic fracturing is implemented. The fracture networks induced by hydraulic fracturing are also responsible for seismic anisotropy in the subsurface. We have shown that seismic anisotropy can have a significant influence on travel-time and amplitude of the recorded seismic waves, thus contributing to larger deviations in source location and moment tensor inversion in microseismic monitoring. These variations in travel-time and amplitude caused by seismic anisotropy can also be used to evaluated the anisotropy of the subsurface, especially for estimating the strength of anisotropy in HTI media using surface array. In vertical downhole array, the travel-time differences of direct P-waves will normally increase with the take-off angle of the seismic rays in VTI media, while the travel-time differences of direct P-waves will normally decrease with the take-off angle of the seismic rays in HTI media. In surface array, the travel-times of direct P-wave exhibit a circular distribution in isotropic and VTI media, while the travel-times of direct P-wave exhibit an ellipse distribution in HTI media. The strength of seismic anisotropy can be estimated by calculating the ratio of the major axis of the ellipse to the minor axis of the ellipse. The direction of the symmetry axis of the HTI media (i.e., the orientation of fracture planes) can also be estimated through identifying the direction of the major axis of the ellipse. The fracturing effect can also be evaluated through anisotropy analysis of different events in hydraulic fracturing. Although the polarization of direct waves is less affected by anisotropy, the deviation in source location will be accumulated into the source mechanism determination and make source mechanism determination problematic. Since we have focused on full waveform modeling in heterogeneous and anisotropic media in this paper, a quantitative analysis of the influence of anisotropy on microseismic source location is not robustly studied.

Compared with surface array, downhole array is more vulnerable to seismic anisotropy. Thus extra care should be taken when conducting microseismic monitoring in anisotropic media using downhole array. Analysing seismic anisotropy of the recorded microseismic data provides a feasible way to evaluate the fracture networks induced by hydraulic fracturing, and can also improve the accuracy of microseismic source location and mechanism characterization.

Acknowledgements We are grateful to the anonymous reviewers who have provided many constructive comments to improve the manuscript. We also wish to thank Institute of Applied Geoscience and Institute of Geophysics and Tectonics, University of Leeds for supporting this work. The work of P. Shi is supported by a China Scholarship Council/University of Leeds scholarship. A. Nowacki is supported by a Leverhulme Early Career Fellowship.

Appendix A Moment tensor source radiation pattern

A seismic moment tensor is the combination of nine generalized couple forces which have three possible directions and act on three possible arms. It can be used to simulate seismic sources which have body-force equivalent given by pairs of forces. The seismic moment tensor source equivalent has been verified by the radiation patterns of teleseismic data and also seismic data obtained very close to the source region (Aki and Richards 2002). A common seismic moment tensor can be expressed as

$$\mathbf{m} = \begin{pmatrix} m_{xx} & m_{xy} & m_{xz} \\ m_{yx} & m_{yy} & m_{yz} \\ m_{zx} & m_{zy} & m_{zz} \end{pmatrix}. \tag{9}$$

The source radiation pattern of P- and S-waves can be derived from the Green's function in an isotropic elastic medium (Aki and Richards 2002). For far-field P-waves, the radiation pattern is given by

$$R_n^p = \gamma_n \gamma_p \gamma_q m_{pq}. \tag{10}$$

For far-field S-waves, the radiation pattern is given by

$$R_n^s = -(\gamma_n \gamma_p - \delta_{np})\gamma_q m_{pq}. \tag{11}$$

In these equations, R_n represents the nth component of the radiation pattern vector for P- or S-wave, γ_p is the direction cosine of the source-receiver unit direction vector, m_{pq} is the moment tensor component. Implicit summation over the repeated index is applied in these equations.

If using the unit basis vectors in spherical coordinates, then we can further obtain the radiation pattern for P-waves (Chapman 2004)

$$\begin{aligned} R^p = &\left(m_{xx}\cos^2\phi + m_{yy}\sin^2\phi + m_{xy}\sin 2\phi\right)\sin^2\theta \\ &+ m_{zz}\cos^2\theta + \left(m_{zx}\cos\phi + m_{yz}\sin\phi\right)\sin 2\theta, \end{aligned} \tag{12}$$

for SV-waves

$$\begin{aligned} R^{sv} = &\frac{1}{2}\left(m_{xx}\cos^2\phi + m_{yy}\sin^2\phi - m_{zz} + m_{xy}\sin 2\phi\right)\sin 2\theta \\ &+ \left(m_{zx}\cos\phi + m_{yz}\sin\phi\right)\cos 2\theta, \end{aligned} \tag{13}$$

for SH-waves

$$R^{sh} = \left(\frac{1}{2}\left(m_{yy} - m_{xx}\right)\sin 2\phi + m_{xy}\cos 2\phi\right)\sin\theta + \left(m_{yz}\cos\phi - m_{zx}\sin\phi\right)\cos\theta, \tag{14}$$

in which θ and ϕ represent the coordinate components (polar angle and azimuth angle) in the spherical coordinates respectively.

Appendix B Analytical solutions in homogeneous isotropic medium

The displacement field in a homogeneous isotropic medium can be obtained by convolving the Green's function with the seismic moment tensor (Aki and Richards 2002, Equation 4.29)

$$
\begin{aligned}
u_n = M_{pq} * G_{np,q} = R_n^{ne} \frac{M_0}{4\pi\rho r^4} \int_{r/v_p}^{r/v_s} \tau S(t-\tau) d\tau + R_n^{ip} \frac{M_0}{4\pi\rho v_p^2 r^2} S\left(t - r/v_p\right) \\
+ R_n^{is} \frac{M_0}{4\pi\rho v_s^2 r^2} S\left(t - r/v_s\right) + R_n^{fp} \frac{M_0}{4\pi\rho v_p^3 r} \dot{S}\left(t - r/v_p\right) + R_n^{fs} \frac{M_0}{4\pi\rho v_s^3 r} \dot{S}\left(t - r/v_s\right),
\end{aligned}
\tag{15}
$$

where u_n is the nth component of displacement field, r is the distance between source point and receiver point, $G_{np,q}$ is the Green's function describing the wave propagation between source and receiver, R_n^{ne}, R_n^{ip}, R_n^{is}, R_n^{fp}, R_n^{fs} are near-field, intermediate-field P-wave, intermediate-field S-wave, far-field P-wave, far-field S-wave radiation pattern respectively. The comma indicates the spatial derivative with respect to the coordinate after the comma (e.g. $G_{np,q} = \partial G_{np}/\partial q$) and the dot above the source time function $S(t)$ indicates the time derivative. Thus, the displacement field in the far-field is proportional to particle velocities at the source. The elastic properties of the medium are described by density ρ, P-wave velocity v_p and S-wave velocity v_s.

The first term in equation 15 is called the near-field term, which is proportional to $r^{-4} \int_{r/v_p}^{r/v_s} \tau S(t-\tau) d\tau$ (hereafter referred to as the proportional part of near-field term). The two middle terms are called the intermediate-field terms, which are proportional to $(vr)^{-2} S(t - r/v)$. The last two terms are called the far-field terms, which are proportional to $v^{-3} r^{-1} \dot{S}(t - r/v)$. Since there is no intermediate-field region where only the intermediate-field terms dominate, it is common to combine the intermediate-field and near-field terms. If a Ricker wavelet $S(t) = (1 - 2\pi^2 f_m^2 t^2) e^{-\pi^2 f_m^2 t^2}$ (f_m is the peak frequency of the wavelet) is used as the source time function, the integration in the near-field term is very small and its peak amplitude is approximately proportional to r/f_m with ratio often smaller than 10^{-6} in SI units. The derivative term of the source time function in the far-field terms is much larger than the Ricker wavelet and its integration, and its peak amplitude is approximately proportional to f_m with an approximate ratio of 6.135 for Ricker wavelet.

Appendix C Distortion of near- and far-field due to source radiation pattern

Normally, the near- and far-field are just defined using source-receiver distance and seismic wavelength. However, through examining equation 15 and numerical experiments, we find that the near- and far-field are also influenced by source radiation patters. Figure 29(a) shows the relative magnitude of peak amplitude of the proportional part of the near-field term, intermediate-field terms and far-field terms at different source-receiver distances. The elastic parameters of the medium used are $v_p = 3500\ m/s$, $v_s = 2000\ m/s$ and $\rho = 2400\ kg/m^3$. The source time function is a Ricker wavelet with a peak frequency of 40 Hz and a time delay of $1.1/f_m$. The X-axis of Figure 29(a) is the ratio of the source-receiver distance to the dominant S-wave wavelength. It is obvious that at a distance larger than three or four dominant S-wave wavelengths, the far-field term dominates the wavefield (with a proportion higher than 95%). This far-field approximation is quite pervasive in microseismic monitoring because of the widely used ray-based methods and relatively high dominant frequencies of the recorded data. Furthermore most focal mechanism inversion methods are also based on the far-field approximation. However, at a distance less than two dominant S-wave wavelengths, the near-field terms and intermediate-field terms will have a non-negligible effect on the whole wavefield, and may even dominate the wavefield, especially when very close to the source region (less than one half the dominant S-wave wavelength). For microseismic downhole monitoring arrays, which are deployed close to the microseismic source area, larger errors may occur due to the significant contribution of the near-field and intermediate-field terms.

The far-field approximation is not only related to the source-receiver distance but also the radiation patterns of the near-field terms (including intermediate-terms hereafter) and far-fields terms. In directions where the strength of the far-field radiation pattern is weaker than the strength of the near-field radiation pattern, the contribution of near-field terms may bias the far-field approximation in the “far” field. Figure 29(b) is a 3D map which shows the far-field distance of a 45° dip-slip double-couple source ($m_{xx} = -m_{zz}$ and other components are 0) in different directions. The elastic property of the medium is the same as before with the moment tensor source radiation pattern displayed in Figure 3. The far-field distance is expressed in terms of S-wave wavelength. The color and shape in the figure shows the distance where the far-field terms will occupy 80% energy in the whole wavefield. Beyond this distance, we can consider that the far-field terms dominate the wavefield. Figure 29(b) reveals an obvious directional feature. If there were no difference in radiation pattern between the far-field and near-field terms, Figure 29(b) would show an uniform spherical distribution in different directions. However the difference in radiation patterns has distorted the scope where the near-field could exert influence on the wavefield. In directions where the near-field radiation pattern is strong and the far-field radiation is weak, the distance in which the near-field terms have a non-negligible influence on the whole wavefield has been extended. The far-field distance in different directions in Figure 29(b) ranges from about 2 times the dominant S-wave wavelength to 12 times the dominant S-wave wavelength. Thus, great care must be taken when receivers have been deployed in these directions. Figure 29(c) shows the variation of relative magnitude in two specific directions for the same double-couple source. The radiation patterns of the near-, intermediate- and far-field terms have been taken into consideration. When considering source radiation pattern, the far-field distance shows strong dependence on directions. The far-field distance has been extended to 12 times the dominant S-wave wavelength in direction of 5° zenith angle and 0° azimuth angle (shown as the dashed lines). The far-field terms need a farther distance to dominate in the whole wavefield. This example demonstrates the far-field distance is not immutable, however is also affected by source radiation patterns. For microseismic monitoring, the receivers are normally deployed near microseismic events, especially for the downhole array. Therefore, the influence of source radiation patterns to far-field distance must be taken into consideration. When source-receiver geometry, source moment tensor and media elastic parameters are defined, the far-field distance in different directions where the far-field approximation is acceptable can be quantitatively evaluated. This will be very helpful for array deployment and data interpretation in microseismic monitoring.

References

Aboudi J (1971) Numerical simulation of seismic sources. Geophysics 36(5):810–821

Aki K, Richards PG (2002) Quantitative seismology, vol 1. University Science Books

Al-Harrasi O, Al-Anboori A, Wüstefeld A, Kendall JM (2011) Seismic anisotropy in a hydrocarbon field estimated from microseismic data. Geophys Prospect

59(2):227–243

Alterman Z, Karal F (1968) Propagation of elastic waves in layered media by finite difference methods. Bull Seismol Soc Am 58(1):367–398

Aminzadeh F, Jean B, Kunz T (1997) 3-D salt and overthrust models. Society of Exploration Geophysicists

Angus D, Aljaafari A, Usher P, Verdon J (2014) Seismic waveforms and velocity model heterogeneity: Towards a full-waveform microseismic location algorithm. J Appl Geophys 111:228–233

Artman B, Podladtchikov I, Witten B (2010) Source location using time-reverse imaging. Geophys Prospect 58(5):861–873

Babuska V, Cara M (1991) Seismic anisotropy in the Earth, vol 10. Springer Science & Business Media

Bachrach R, Sengupta M, Salama A, Miller P (2009) Reconstruction of the layer anisotropic elastic parameters and high-resolution fracture characterization from p-wave data: a case study using seismic inversion and bayesian rock physics parameter estimation. Geophys Prospect 57(2):253–262

Bakulin A, Grechka V, Tsvankin I (2000) Estimation of fracture parameters from reflection seismic data—part i: Hti model due to a single fracture set. Geophysics 65(6):1788–1802

Baysal E, Kosloff DD, Sherwood JW (1983) Reverse time migration. Geophysics 48(11):1514–1524

Bohlen T (2002) Parallel 3-d viscoelastic finite difference seismic modelling. Comput Geosci 28(8):887–899

Boyd OS (2006) An efficient matlab script to calculate heterogeneous anisotropically elastic wave propagation in three dimensions. Comput Geosci 32(2):259–264

Brzak K, Gu YJ, Ökeler A, Steckler M, Lerner-Lam A (2009) Migration imaging and forward modeling of microseismic noise sources near southern Italy. Geochem Geophys Geosyst 10(1)

Cesca S, Rohr A, Dahm T (2013) Discrimination of induced seismicity by full moment tensor inversion and decomposition. J Seismol 17(1):147–163

Chambers K, Dando BD, Jones GA, Velasco R, Wilson SA (2014) Moment tensor migration imaging. Geophys Prospect 62(4):879–896

Chapman C (2004) Fundamentals of seismic wave propagation. Cambridge university press

Coutant O, Virieux J, Zollo A (1995) Numerical source implementation in a 2d finite difference scheme for wave propagation. Bull Seismol Soc Am 85(5):1507–1512

Crampin S, Peacock S (2008) A review of the current understanding of seismic shear-wave splitting in the earth's crust and common fallacies in interpretation. Wave Motion 45(6):675–722

Dong Z, McMechan GA (1995) 3-d viscoelastic anisotropic modeling of data from a multicomponent, multiazimuth seismic experiment in northeast texas. Geophysics 60(4):1128–1138

Foulger G, Julian B, Hill D, Pitt A, Malin P, Shalev E (2004) Non-double-couple microearthquakes at long valley caldera, california, provide evidence for hydraulic fracturing. J Volcanol Geotherm Res 132(1):45–71

Gajewski D, Tessmer E (2005) Reverse modelling for seismic event characterization. Geophys J Int 163(1):276–284

Graves RW (1996) Simulating seismic wave propagation in 3d elastic media using staggered-grid finite differences. Bull Seismol Soc Am 86(4):1091–1106

Grechka V, Yaskevich S (2013a) Azimuthal anisotropy in microseismic monitoring: A bakken case study. Geophysics 79(1):KS1–KS12

Grechka V, Yaskevich S (2013b) Inversion of microseismic data for triclinic velocity models. Geophys Prospect 61(6):1159–1170

Grechka V, Singh P, Das I (2011) Estimation of effective anisotropy simultaneously with locations of microseismic events. Geophysics 76(6):WC143–WC155

Helbig K, Thomsen L (2005) 75-plus years of anisotropy in exploration and reservoir seismics: A historical review of concepts and methods. Geophysics

Hobro J, Williams M, Calvez JL (2016) The finite-difference method in microseismic modeling: Fundamentals, implementation, and applications. The Leading Edge 35(4):362–366

Holberg O (1987) Computational aspects of the choice of operator and sampling interval for numerical differentiation in large-scale simulation of wave phenomena. Geophys Prospect 35(6):629–655

Jin S, Jiang F, Zhu X (2013) Viscoelastic modeling with simultaneous microseismic sources. In: SEG Technical Program Expanded Abstracts 2013, Society of Exploration Geophysicists, pp 3355–3359

Johnston JE, Christensen NI (1995) Seismic anisotropy of shales. J Geophys Res 100(B4):5991–6003

Jost Mu, Herrmann R (1989) A student's guide to and review of moment tensors. Seismol Res Lett 60(2):37–57

Julian BR, Miller AD, Foulger G (1998) Non-double-couple earthquakes 1. theory. Rev Geophys 36(4):525–549

Kawakatsu H, Montagner JP (2008) Time-reversal seismic-source imaging and moment-tensor inversion. Geophys J Int 175(2):686–688

Kelly K, Ward R, Treitel S, Alford R (1976) Synthetic seismograms: A finite-difference approach. Geophysics 41(1):2–27

Kendall JM, Fisher Q, Crump SC, Maddock J, Carter A, Hall S, Wookey J, Valcke S, Casey M, Lloyd G, et al (2007) Seismic anisotropy as an indicator of reservoir quality in siliciclastic rocks. Geol Soc London Spec Publ 292(1):123–136

King A, Talebi S (2007) Anisotropy effects on microseismic event location. Pure Appl Geophys 164(11):2141–2156

Kosloff D, Queiroz Filho A, Tessmer E, Behle A (1989) Numerical solution of the acoustic and elastic wave equations by a new rapid expansion method. Geophys Prospect 37(4):383–394

Lele SK (1992) Compact finite difference schemes with spectral-like resolution. J Comput Phys 103(1):16–42

Li D, Helmberger D, Clayton RW, Sun D (2014) Global synthetic seismograms using a 2-d finite-difference method. Geophys J Int 197(2):1166–1183

Li H, Wang R, Cao S (2015) Microseismic forward modeling based on different focal mechanisms used by the seismic moment tensor and elastic wave equation. J Geophys Eng 12(2):155

Li J, Sadi Kuleli H, Zhang H, Nafi Toksöz M (2011) Focal mechanism determination of induced microearthquakes in an oil field using full waveforms from shallow and deep seismic networks. Geophysics 76(6):WC87–WC101

Linzer L, Mhamdi L, Schumacher T (2015) Application of a moment tensor inversion code developed for mining-induced seismicity to fracture monitoring of civil engineering materials. J Appl Geophys 112:256–267

Lisitsa V, Vishnevskiy D (2010) Lebedev scheme for the numerical simulation of wave propagation in 3d anisotropic elasticity‡. Geophys Prospect 58(4):619–635

Liu Y, Sen MK (2009) An implicit staggered-grid finite-difference method for seismic modelling. Geophys J Int 179(1):459–474

Long MD, Silver PG (2009) Shear wave splitting and mantle anisotropy: measurements, interpretations, and new directions. Surv Geophys 30(4-5):407–461

Michéa D, Komatitsch D (2010) Accelerating a three-dimensional finite-difference wave propagation code using gpu graphics cards. Geophys J Int 182(1):389–402

Miller AD, Foulger G, Julian BR (1998) Non-double-couple earthquakes 2. observations. Rev Geophys 36(4):551–568

Moczo P, Kristek J, Vavryčuk V, Archuleta RJ, Halada L (2002) 3d heterogeneous staggered-grid finite-difference modeling of seismic motion with volume harmonic and arithmetic averaging of elastic moduli and densities. Bull Seismol Soc Am 92(8):3042–3066

Moczo P, Kristek J, Gális M (2014) The finite-difference modelling of earthquake motions: Waves and ruptures. Cambridge University Press

Montagner JP (1998) Where can seismic anisotropy be detected in the earth's mantle? in boundary layers... Pure Appl Geophys 151(2-4):223

Nakata N, Beroza GC (2016) Reverse time migration for microseismic sources using the geometric mean as an imaging condition. Geophysics 81(2):KS51–KS60

Narayan J (2001) Site-specific strong ground motion prediction using 2.5-d modelling. Geophys J Int 146(2):269–281

Nowacki A, Wookey J, Kendall JM (2011) New advances in using seismic anisotropy, mineral physics and geodynamics to understand deformation in the lowermost mantle. J Geodyn 52(3):205–228

O'Brien G, Lokmer I, De Barros L, Bean CJ, Saccorotti G, Metaxian JP, Patané D (2011) Time reverse location of seismic long-period events recorded on mt etna. Geophys J Int 184(1):452–462

Panza GF, Saraò A (2000) Monitoring volcanic and geothermal areas by full seismic moment tensor inversion: Are non-double-couple components always artefacts of modelling? Geophys J Int 143(2):353–364

Pitarka A (1999) 3d elastic finite-difference modeling of seismic motion using staggered grids with nonuniform spacing. Bull Seismol Soc Am 89(1):54–68

Robertsson JO, van Manen DJ, Schmelzbach C, Van Renterghem C, Amundsen L (2015) Finite-difference modelling of wavefield constituents. Geophys J Int 203(2):1334–1342

Rössler D, Rümpker G, Krüger F (2004) Ambiguous moment tensors and radiation patterns in anisotropic media with applications to the modeling of earthquake mechanisms in w-bohemia. Stud Geophys Geod 48(1):233–250

Rüger A (1997) P-wave reflection coefficients for transversely isotropic models with vertical and horizontal axis of symmetry. Geophysics 62(3):713–722

Sadri M, Riahi M (2010) Ray tracing and amplitude calculation in anisotropic layered media. Geophys J Int 180(3):1170–1180

Saenger EH, Gold N, Shapiro SA (2000) Modeling the propagation of elastic waves using a modified finite-difference grid. Wave Motion 31(1):77–92

Saenger EH, Kocur GK, Jud R, Torrilhon M (2011) Application of time reverse modeling on ultrasonic non-destructive testing of concrete. Appl Math Model 35(2):807–816

Sayers CM (1998) Misalignment of the orientation of fractures and the principal axes for p and s waves in rocks containing multiple non-orthogonal fracture sets. Geophys J Int 133(2):459–466

Schoenberg M, Sayers CM (1995) Seismic anisotropy of fractured rock. Geophysics 60(1):204–211

Sheriff RE, Geldart LP (1995) Exploration seismology. Cambridge university press

Šílenỳ J, Milev A (2008) Source mechanism of mining induced seismic events—resolution of double couple and non double couple models. Tectonophysics 456(1):3–15

Šílenỳ J, Hill DP, Eisner L, Cornet FH (2009) Non–double-couple mechanisms of microearthquakes induced by hydraulic fracturing. J Geophys Res 114(B8)

Sone H, Zoback MD (2013) Mechanical properties of shale-gas reservoir rocks—part 1: Static and dynamic elastic properties and anisotropy. Geophysics

Song F, Toksöz MN (2011) Full-waveform based complete moment tensor inversion and source parameter estimation from downhole microseismic data for hydrofracture monitoring. Geophysics 76(6):WC103–WC116

Steiner B, Saenger EH, Schmalholz SM (2008) Time reverse modeling of low-frequency microtremors: Application to hydrocarbon reservoir localization. Geophys Res Lett 35(3)

Stierle E, Vavryčuk V, Kwiatek G, Charalampidou EM, Bohnhoff M (2016) Seismic moment tensors of acoustic emissions recorded during laboratory rock deformation experiments: sensitivity to attenuation and anisotropy. Geophys J Int 205(1):38–50

Tarantola A (2005) Inverse problem theory and methods for model parameter estimation. SIAM

Teanby N, Kendall JM, Jones R, Barkved O (2004) Stress-induced temporal variations in seismic anisotropy observed in microseismic data. Geophys J Int 156(3):459–466

Thomsen L (1986) Weak elastic anisotropy. Geophysics 51(10):1954–1966

Tromp J, Komattisch D, Liu Q (2008) Spectral-element and adjoint methods in seismology. Commun Comput Phys 3(1):1–32

Tsvankin I (1997) Anisotropic parameters and p-wave velocity for orthorhombic media. Geophysics 62(4):1292–1309

Usher P, Angus D, Verdon J (2013) Influence of a velocity model and source frequency on microseismic waveforms: some implications for microseismic locations. Geophys Prospect 61(s1):334–345

Vavryčuk V (2004) Inversion for anisotropy from non-double-couple components of moment tensors. J Geophys Res 109(B7)

Vavryčuk V (2005) Focal mechanisms in anisotropic media. Geophys J Int 161(2):334–346

Vavryčuk V (2007) On the retrieval of moment tensors from borehole data. Geophys Prospect 55(3):381–391

Verdon J, Kendall JM, Wüstefeld A (2009) Imaging fractures and sedimentary fabrics using shear wave splitting measurements made on passive seismic data. Geophys J Int 179(2):1245–1254

Verdon JP, Kendall J, et al (2011) Detection of multiple fracture sets using observations of shear-wave splitting in microseismic data. Geophysical Prospecting 59(4):593–608

Vernik L, Liu X (1997) Velocity anisotropy in shales: A petrophysical study. Geophysics 62(2):521–532

Vidale JE (1995) Near-field deformation seen on distant broadband. Geophys Res Lett 22(1):1–4

Virieux J (1984) Sh-wave propagation in heterogeneous media: Velocity-stress finite-difference method. Geophysics 49(11):1933–1942

Virieux J (1986) P-sv wave propagation in heterogeneous media: Velocity-stress finite-difference method. Geophysics 51(4):889–901

Virieux J, Operto S (2009) An overview of full-waveform inversion in exploration geophysics. Geophysics 74(6):WCC1–WCC26

Walker AM, Wookey J (2012) Msat—a new toolkit for the analysis of elastic and seismic anisotropy. Comput Geosci 49:81–90

Wang S, Li XY, Qian Z, Di B, Wei J (2007) Physical modelling studies of 3-d p-wave seismic for fracture detection. Geophys J Int 168(2):745–756

Wang Y (2013) Seismic ray tracing in anisotropic media: A modified newton algorithm for solving highly nonlinear systems. Geophysics 79(1):T1–T7

Wang Z (2002) Seismic anisotropy in sedimentary rocks, part 2: Laboratory data. Geophysics 67(5):1423–1440

Warpinski NR, Waltman CK, Du J, Ma Q, et al (2009) Anisotropy effects in microseismic monitoring. In: SPE Annual Technical Conference and Exhibition, Society of Petroleum Engineers

Wong J, Manning PM, Han L, Bancroft JC (2011) Synthetic microseismic datasets. CSEG RECORDER

Wuestefeld A, Al-Harrasi O, Verdon JP, Wookey J, Kendall JM (2010) A strategy for automated analysis of passive microseismic data to image seismic anisotropy and fracture characteristics. Geophys Prospect 58(5):755–773

Xu Y (2012) Analysis of p-wave seismic response for fracture detection: Modelling and case studies. PhD thesis, The University of Edinburgh

Xuan R, Sava P (2010) Probabilistic microearthquake location for reservoir monitoring. Geophysics 75(3):MA9–MA26

Yan B, Yuan S, Wang S, OuYang Y, Wang T, Shi P (2016) Improved eigenvalue-based coherence algorithm with dip scanning. Geophysics 82(2):V95–V103

Yao G, Wu D, Debens HA (2016) Adaptive finite difference for seismic wavefield modelling in acoustic media. Sci Rep 6:30,302

Yomogida K, Etgen JT (1993) 3-d wave propagation in the los angeles basin for the whittier-narrows earthquake. Bull Seismol Soc Am 83(5):1325–1344

Yuan S, Wang S, Sun W, Miao L, Li Z (2014) Perfectly matched layer on curvilinear grid for the second-order seismic acoustic wave equation. Explor Geophys 45(2):94–104

Yuan S, Wang S, Luo C, He Y (2015) Simultaneous multitrace impedance inversion with transform-domain sparsity promotion. Geophysics 80(2):R71–R80

Zhang JH, Yao ZX (2013) Optimized explicit finite-difference schemes for spatial derivatives using maximum norm. J Comput Phys 250:511–526

Zhang Y, Eisner L, Barker W, Mueller MC, Smith KL (2013) Effective anisotropic velocity model from surface monitoring of microseismic events. Geophys Prospect 61(5):919–930

Zienkiewicz OC, Taylor RL, Taylor RL (1977) The finite element method, vol 3. McGraw-hill London

Table 1 Memory cost for storing elastic parameters (including density of the medium) of different types of medium. M represents the model size

Medium type	Memory cost
Isotropic	3M
VTI/HTI	6M
TTI	8M
Orthorhombic	10M
Monoclinic	14M
Triclinic	22M

Table 2 Simulation time (in second) of 10 time steps for different grid sizes and number of cores in anisotropic media.

Model size	1 core	2 cores	4 cores	8 cores	16 cores
100*100*100	1.7	0.9	0.5	0.3	0.2
200*200*200	15.9	7.9	4.0	2.1	1.2
400*400*400	140.1	70.5	35.5	18.3	10.1
600*600*600	617.5	310.0	150.5	75.3	39.6
800*800*800	1356.6	669.5	321.3	176.3	93.6

Table 3 Modeling parameters and CPU times (hour/CPU) for different main frequencies of the source time function.

f (Hz)	Δh (m)	Δt (s)	Grid size	Time steps	Memory cost (Gb)	CPU time
10	31.35	0.00220	$96 \times 96 \times 96$	1841	0.046	0.08
20	15.67	0.00110	$192 \times 192 \times 192$	3681	0.369	1.25
40	7.84	0.00054	$383 \times 383 \times 383$	7361	2.930	19.88
80	3.92	0.00027	$766 \times 766 \times 766$	14721	23.441	318.04
100	3.13	0.00021	$957 \times 957 \times 957$	18402	45.711	775.29
120	2.61	0.00018	$1149 \times 1149 \times 1149$	22082	79.113	1610.10
150	2.09	0.00014	$1436 \times 1436 \times 1436$	27602	154.437	3928.80

Table 4 Elastic parameters of layered isotropic model

Layer	Thickness (m)	Vp (m/s)	Vs (m/s)	Density (kg/m^3)
1	750	3724	1944	2450
2	1000	4640	2583	2490
3	750	5854	3251	2680

Table 5 Source location results in isotropic, VTI and HTI media using surface array. The source location is determined by minimising the difference between the recorded arrival times and calculated traveltimes of a given velocity model. *Δ* means the difference between estimated and correct value. Cumulative residual is the overall cumulative residuals of arrival times for all receivers during source location

Medium	ΔX (m)	ΔY (m)	ΔZ (m)	ΔT_0 (s)	Cumulative residual (s)
ISO	0	0	0	0	0.0165
VTI	0	0	570	-0.1195	0.0246
HTI	0	0	190	-0.0614	0.2344

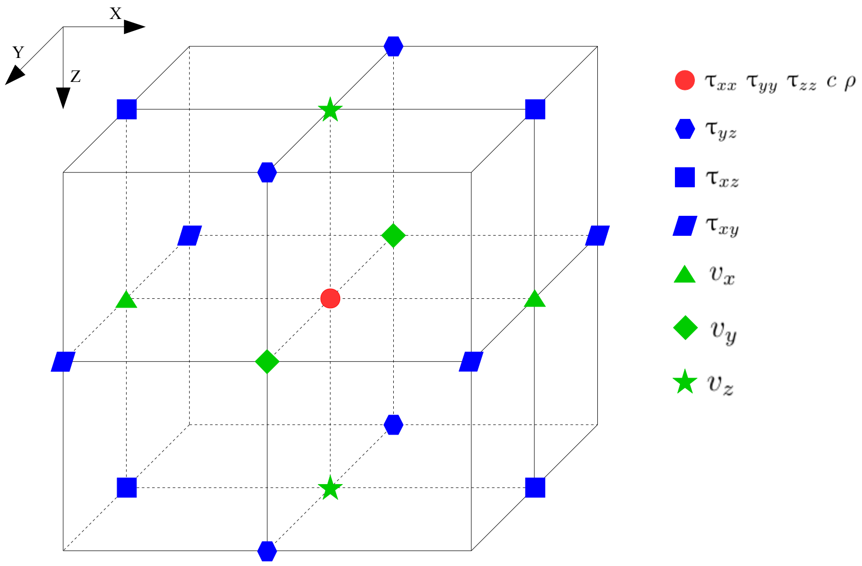

Fig. 1 Schematic representation of standard staggered-grid. v_x, v_y, v_z represent the particle velocity components along x-, y- and z-directions respectively; $\tau_{xx}, \tau_{yy}, \tau_{zz}, \tau_{yz}, \tau_{xz}, \tau_{xy}$ represent six components of the stress tensor; c and ρ represent the elastic tensor and density of the media

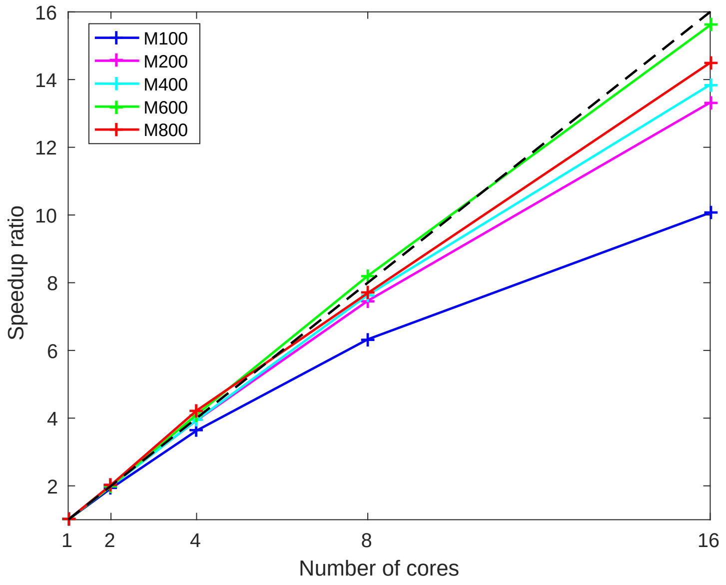

(a)

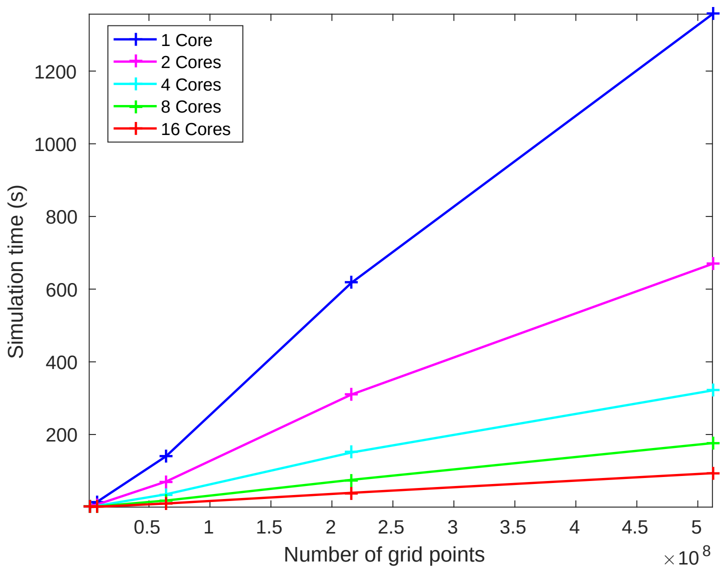

(b)

Fig. 2 (a) Variation of speedup ratios with the number of computer cores for different model sizes. Blue, magenta, cyan, green and red lines show the simulation times with model size of $100 \times 100 \times 100$, $200 \times 200 \times 200$, $400 \times 400 \times 400$, $600 \times 600 \times 600$ and $800 \times 800 \times 800$ respectively. (b) Variation of simulation times with the number of grid points for different number of compute cores. Blue, magenta, cyan, green and red lines show the simulation times with computer cores of 1, 2, 4, 8 and 16 respectively

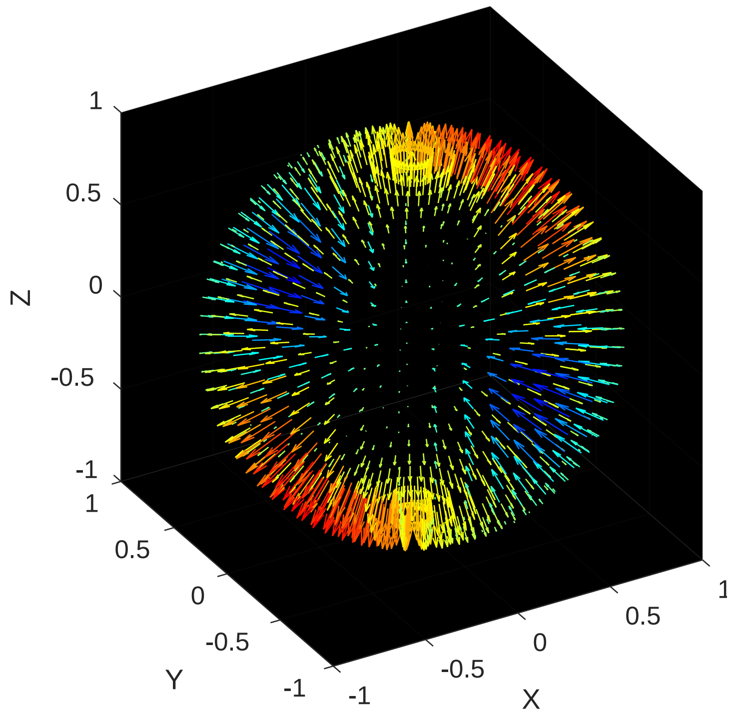

(a)

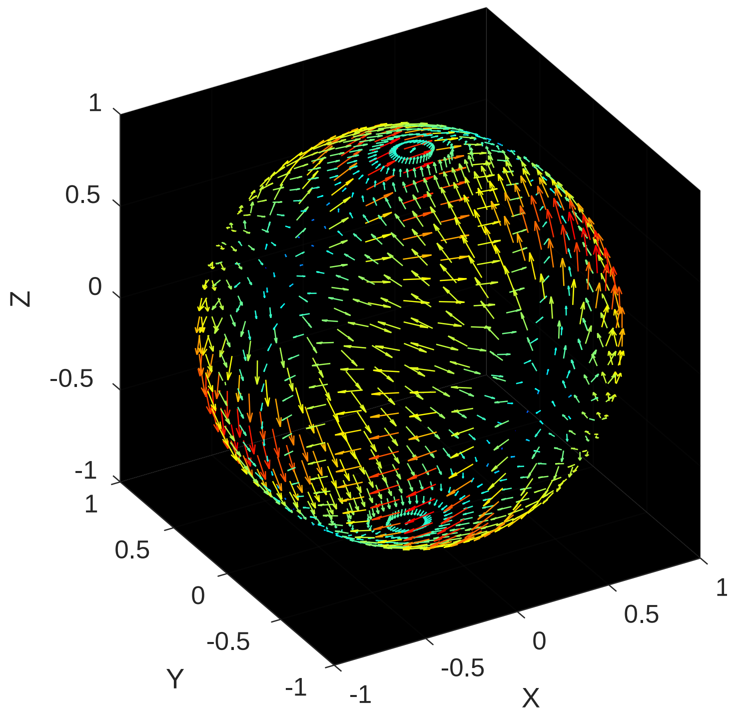

(b)

Fig. 3 The far-field P-wave (a) and S-wave (b) radiation patterns of the non-double-couple moment tensor source (expressed in equation 7). The vectors exhibit the polarization direction of the P- and S-waves and the color and length of the vectors represent the polarization strength. Red color represents positive polarization, blue color represents negative polarization. X, Y and Z axes show the 3D spatial coordinates which are normalized to 1

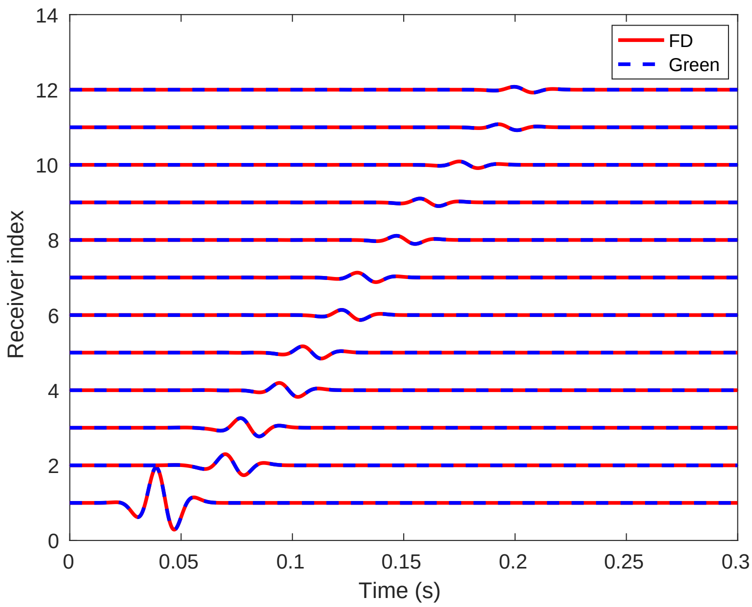

(a)

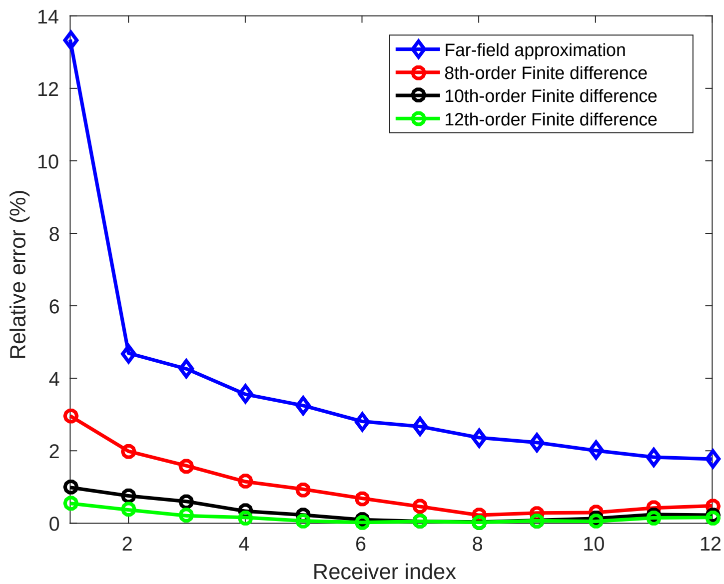

(b)

Fig. 4 (a) Synthetic seismograms (displacement in Y direction only) recorded by twelve receivers deployed in different directions and positions, with the FD results in solid red line overlaying the analytical solutions obtained by Green's function (equation 15 in Appendix B) in dashed blue line. (b) Relative error of the peak amplitude of FD modeling and far-field approximation with respect to analytical solutions for the twelve FD records, with FD method in red, black and green lines and far-field approximation in blue line. Red, black and green color represent the 8th-, 10th- and 12th-order FD results respectively

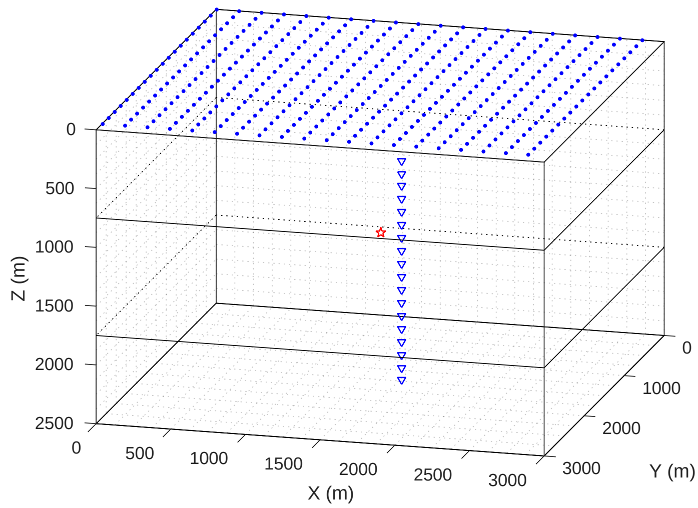

(a)

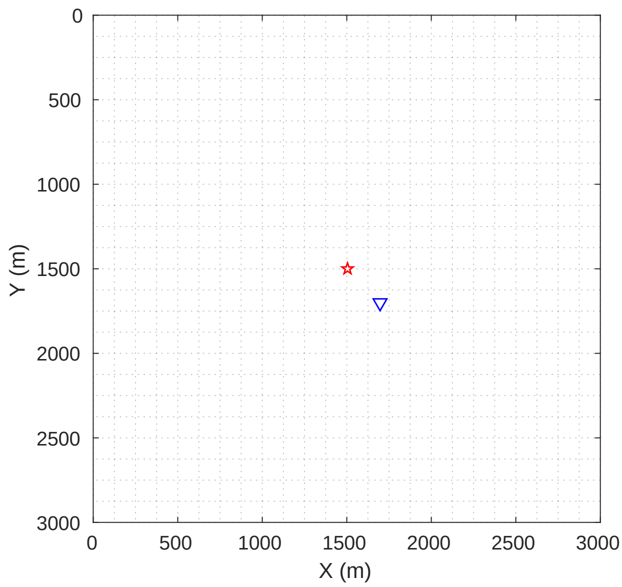

(b)

Fig. 5 (a) Schematic representation of the layered model and the recording arrays. The red star represents microseismic source, the blue points represent surface arrays, the blue triangles represent downhole arrays. The microseismic source is placed in the middle of the model. (b) Surface projection of the source and downhole array

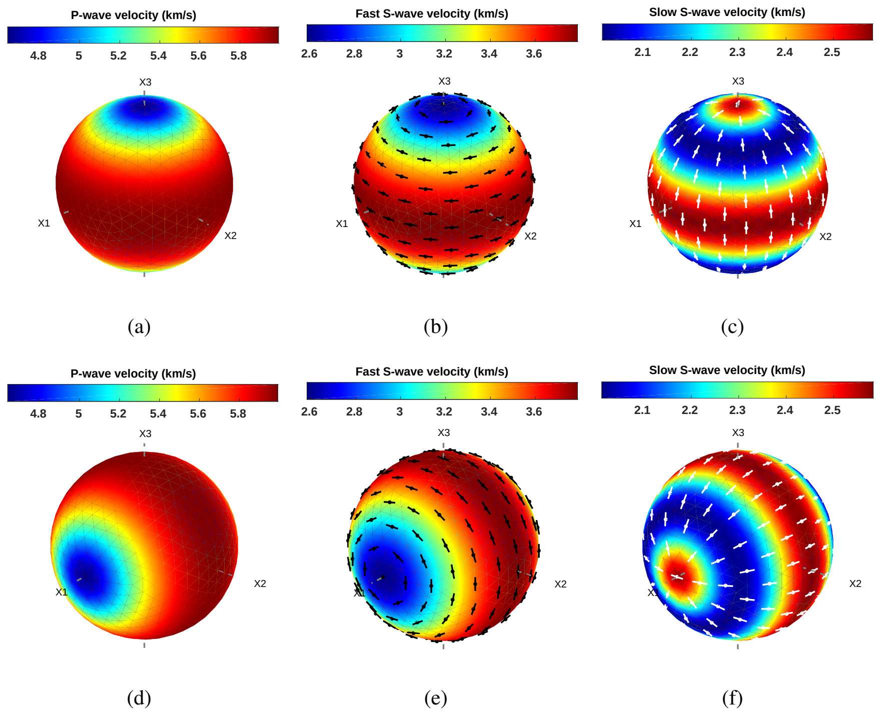

Fig. 6 Variation of the (c) P-wave, (d) fast S-wave and (e) slow S-wave velocity in VTI medium along different propagation directions. Variation of the (f) P-wave, (g) fast S-wave and (h) slow S-wave velocity in HTI medium along different propagation directions. The black and white markers indicate the fast and slow S-wave polarization directions, respectively. Figures created using MSAT (Walker and Wookey 2012)

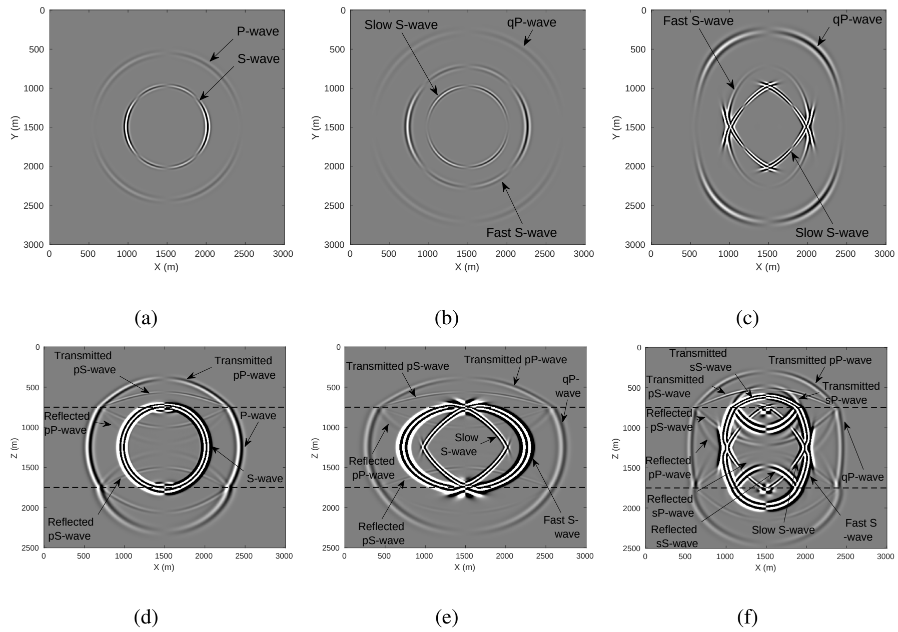

Fig. 7 Horizontal slices of velocity component in Y direction for the (a) isotropic, (b) VTI and (c) HTI model. The horizontal slices are taken at time of 0.23 s and depth of microseismic source (z=1250 m). Vertical slices of velocity component in Y direction for the (d) isotropic, (e) VTI and (f) HTI model. The vertical slices are taken at a time of 0.23 s and lateral position of y=1500 m. Dashed lines show boundaries of different layers

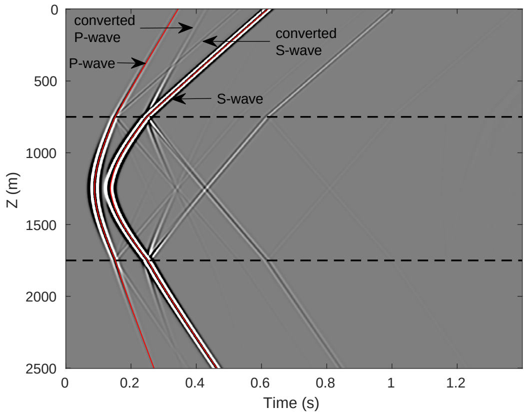

(a)

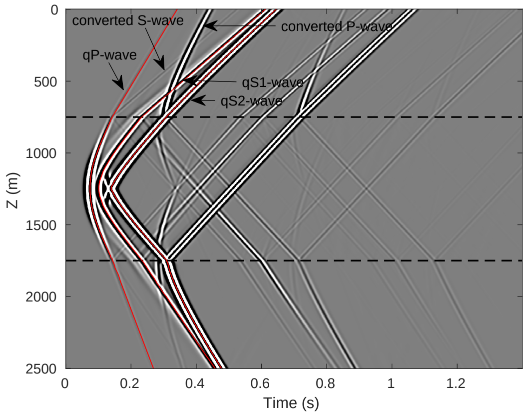

(b)

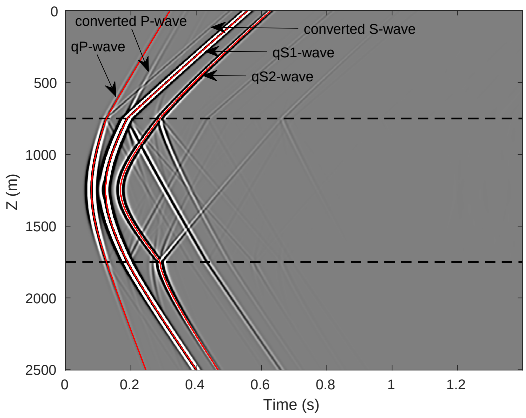

(c)

Fig. 8 The recorded seismograms in downhole array for the (a) isotropic, (b) VTI and (c) HTI model. Vertical axis shows the position of geophones and horizontal axis shows recording time. Red dotted lines represent the automatically picked direct P- and S-wave wavefronts; dashed lines show boundaries of different layers

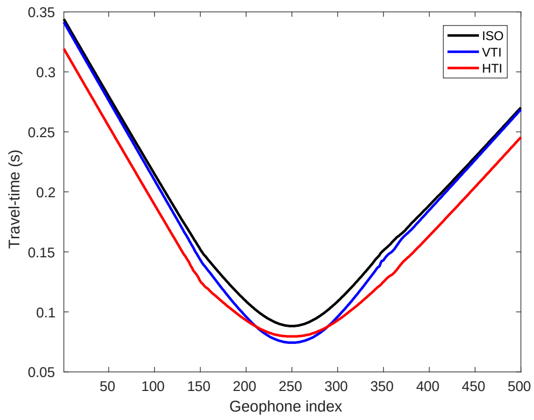

(a)

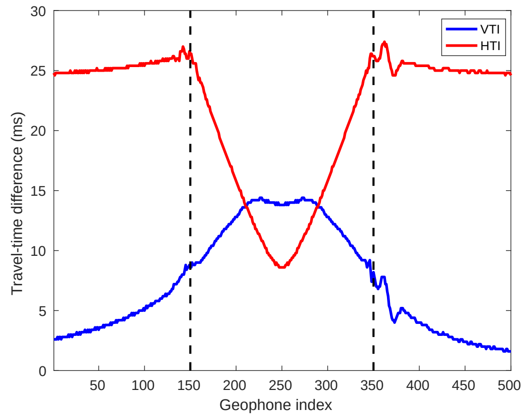

(b)

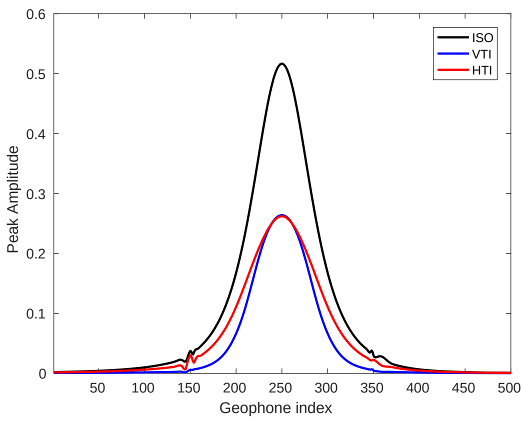

(c)

Fig. 9 Comparison of travel-times and peak amplitudes of the direct P-wave for three modelings. Dark solid line represents value in the isotropic model; blue solid line represents value in the VTI model; red solid line represents value in the HTI model; dashed lines show boundaries of the layers (geophone 150 and geophone 350 are placed at layer boundary, geophone 250 is at the same depth of microseismic source). (a) Travel-times of the direct P-wave. (b) Travel-time differences with respect to the isotropic case. (c) Peak amplitudes of the direct P-wave

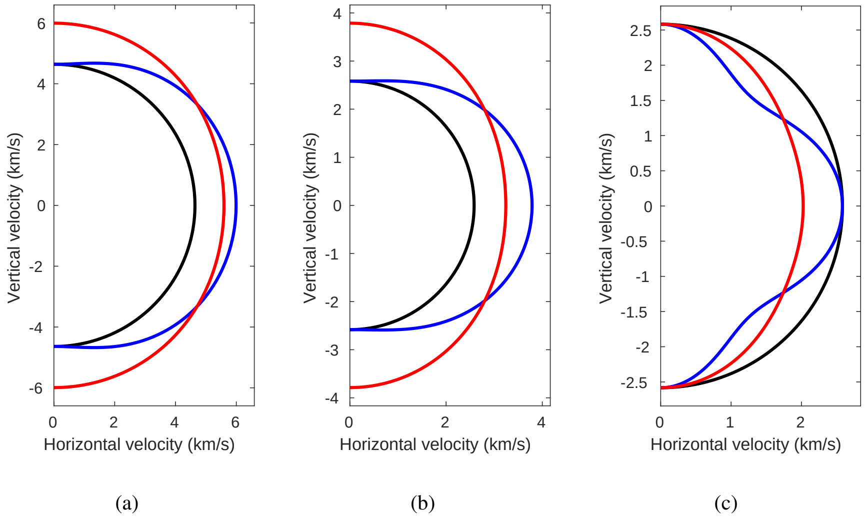

Fig. 10 Velocity surfaces of the P-, fast S- and slow S-waves, calculated in the same profile of the down-hole array. The dark line represents the isotropic model; blue line represents the VTI model; red line represents the HTI model. For the isotropic model, there is only one S-wave mode, whose velocity is used in both fast and slow S-wave surface. (a) P-wave velocity surface; (b) fast S-wave velocity surface; (c) slow S-wave velocity surface. The velocity surface is the representation of directionally-dependent body-wave phase velocities, and calculated through Christoffel equation

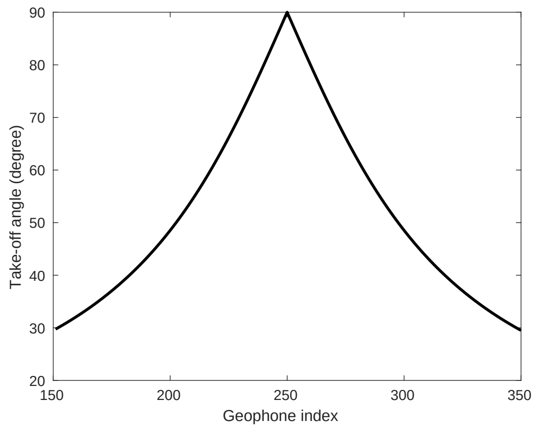

(a)

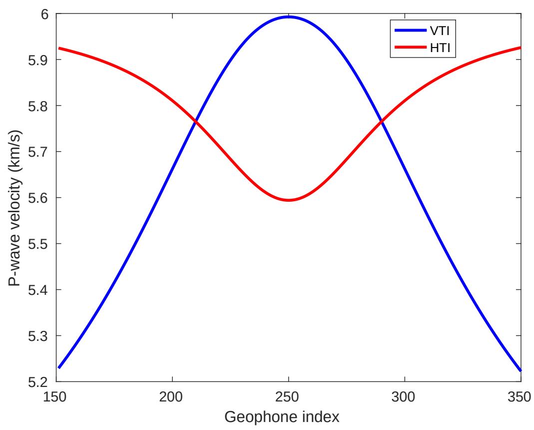

(b)

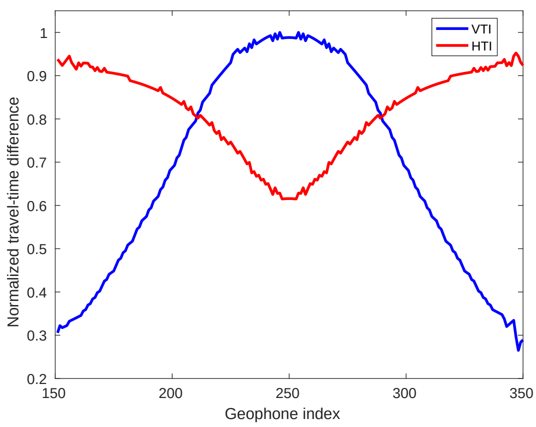

(c)

Fig. 11 (a) Relationship between the take-off angle and geophone index. (b) Velocity variation of the P-wave for downhole geophones at the second layer. (c) Normalized travel-time differences of the direct P-wave for downhole geophones at the second layer. The effect of the ray-path has been considered and eliminated. The small wigglings come from numerical artefacts of the automatic arrival time picking algorithm

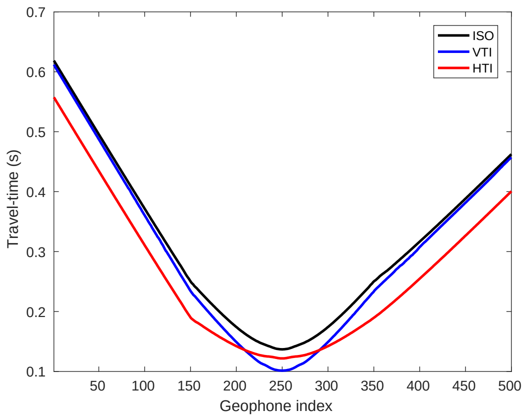

(a)

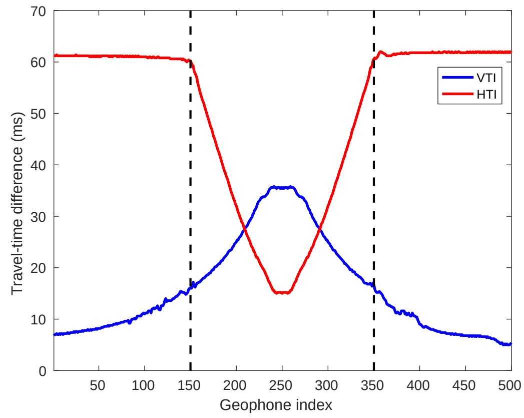

(b)

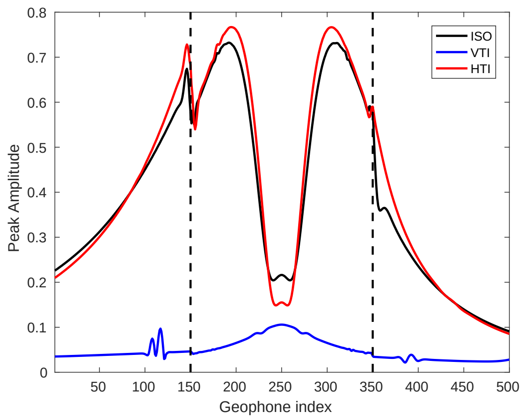

(c)

Fig. 12 Comparison of travel-times and peak amplitudes of the direct fast S-wave (S-wave in the isotropic case) for three modeling examples. The figure description is analogous to figure 9. The small wiggling in the figure are caused by picking error introduced by interference of different waves. The sudden jump of peak amplitudes near the layer boundaries is caused by sudden change in elastic parameters or wave impedance between layers. (a) Travel-times of the direct S-wave or fast S-wave. (b) Travel-time differences with respect to isotropic case. (c) Peak amplitudes of the direct S-wave or fast S-wave

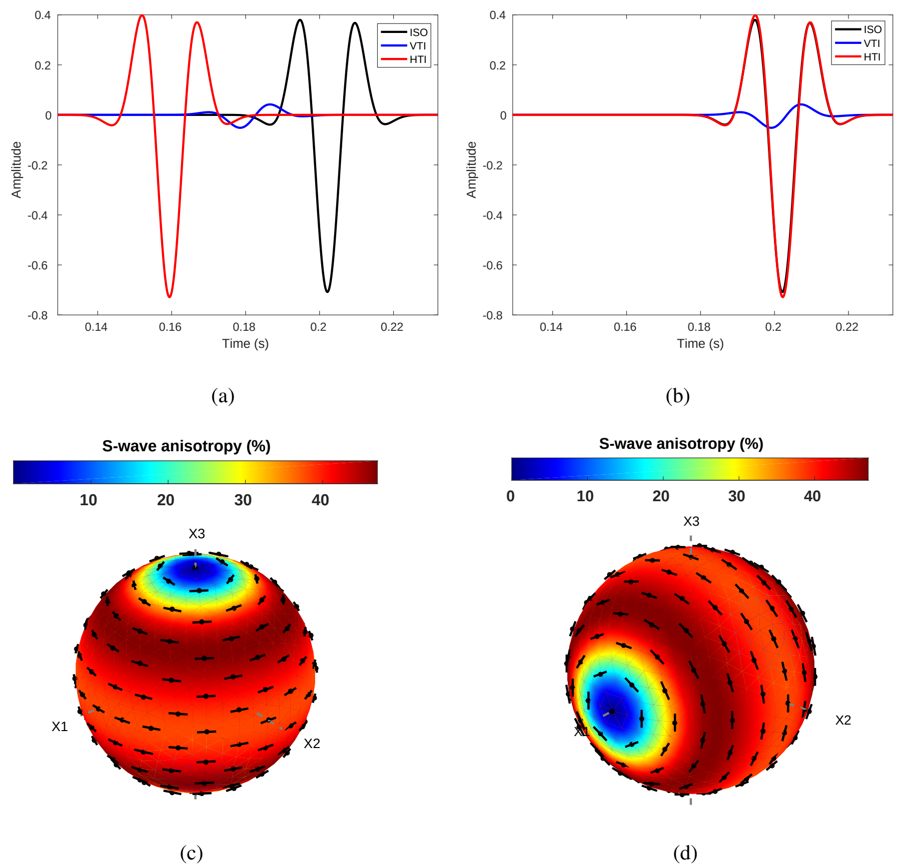

Fig. 13 Waveform of the direct fast S-wave (S-wave in isotropic case) before (a) and after (b) time alignment at downhole geophone 180. Variation of S-wave anisotropy along different propagation directions in the (c) VTI and (d) HTI medium

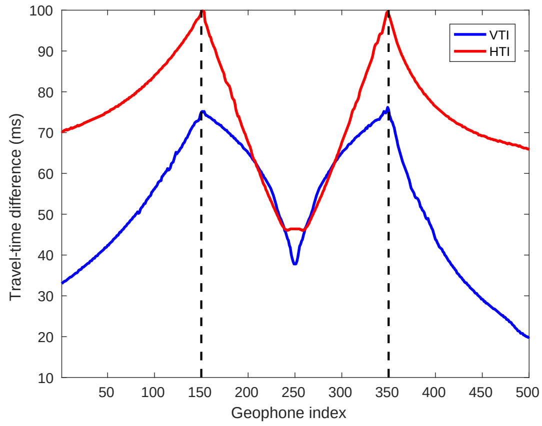

(a)

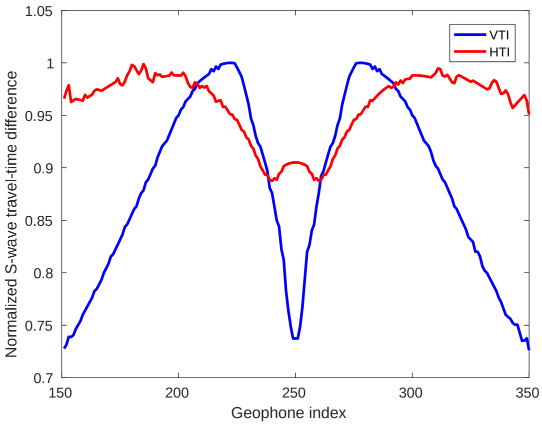

(b)

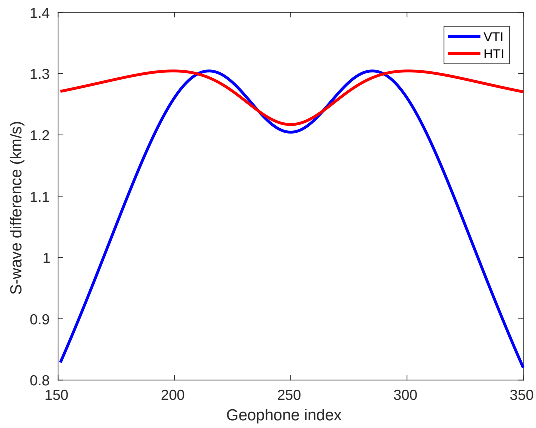

(c)

Fig. 14 (a) Travel-time differences between the fast S-wave and slow S-wave in the VTI and HTI model. (b) Normalized travel-time differences between the fast S-wave and slow S-wave in the VTI and HTI model at the second layer. The effect of the ray-path has been considered and eliminated. (c) Velocity difference between the fast S-wave and slow S-wave in the VTI and HTI model at the second layer

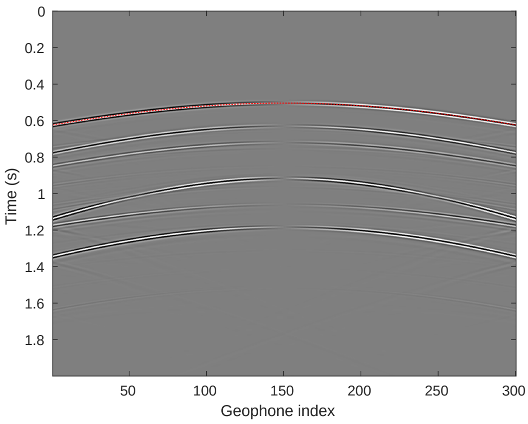

(a)

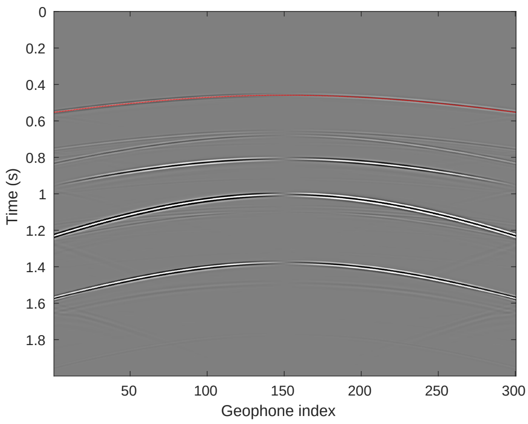

(b)

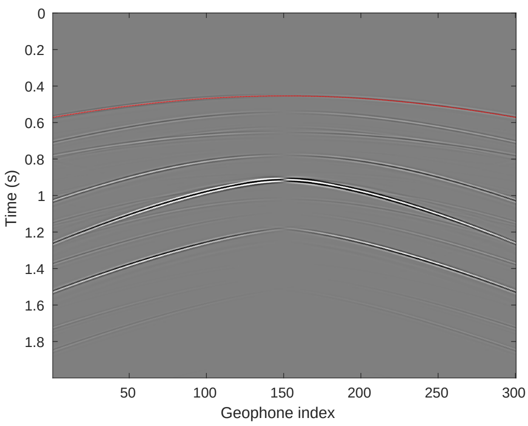

(c)

Fig. 15 Recorded seismic profiles along the first line in the Y direction for the (a) isotropic, (b) VTI and (c) HTI models using surface array. These profiles are recorded at the first receiver line in Y direction. The direct P-wave has been automatically picked and annotated with red line in the figure

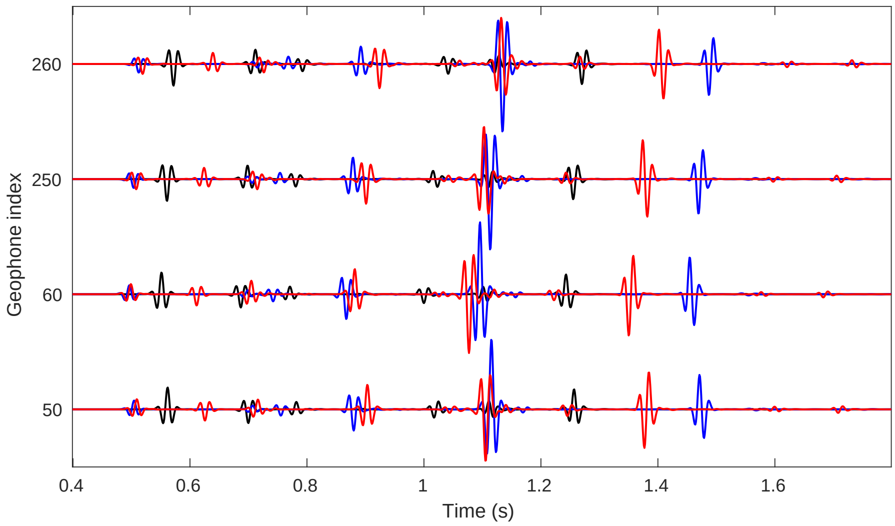

Fig. 16 Shown are four traces extracted form figure 15 with the isotropic case in dark line, the VTI case in blue line and the HTI case in red line

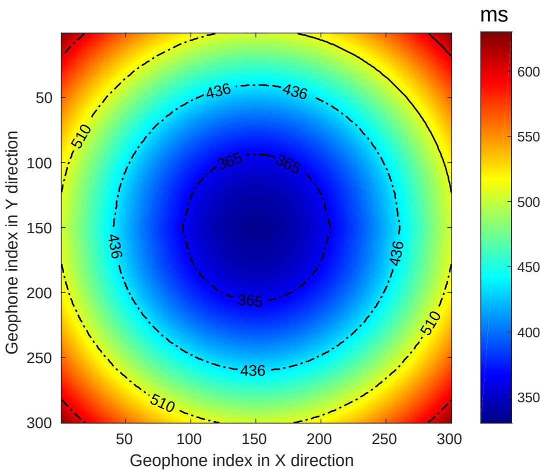

(a)

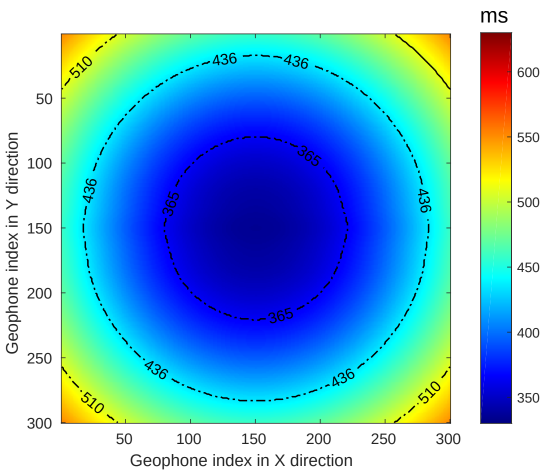

(b)

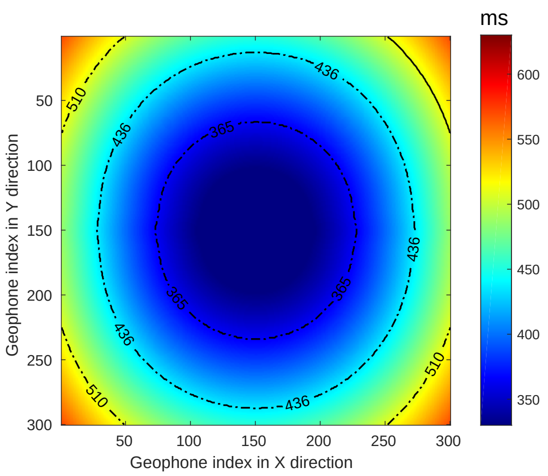

(c)

Fig. 17 Travel-times of the direct P-wave in the (a) isotropic, (b) VTI and (c) HTI models for the surface array. The unit of time in these figures is millisecond. The contour lines of travel-times are also displayed in the figure

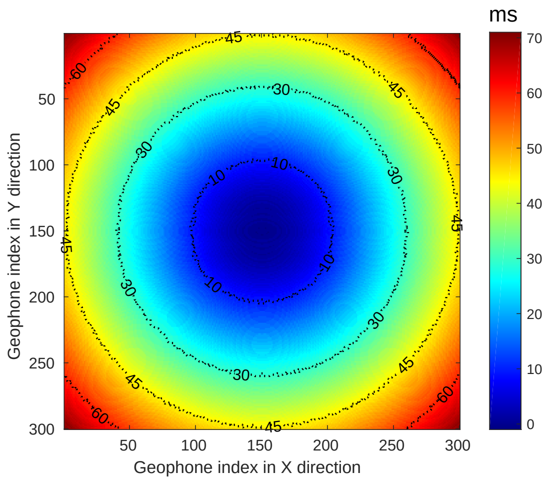

(a)

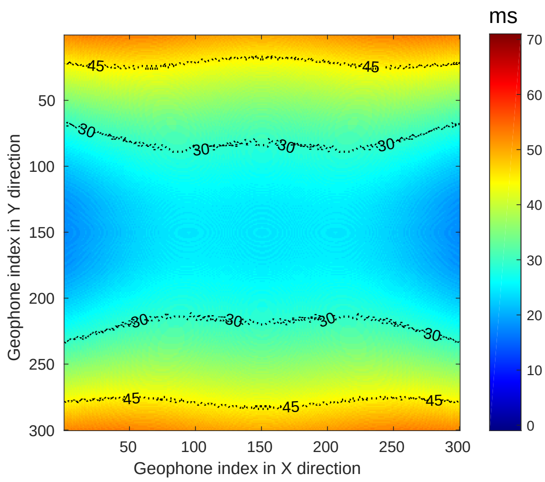

(b)

Fig. 18 Travel-time differences of the direct P-wave with respect to the isotropic case. (a) VTI model; (b) HTI model

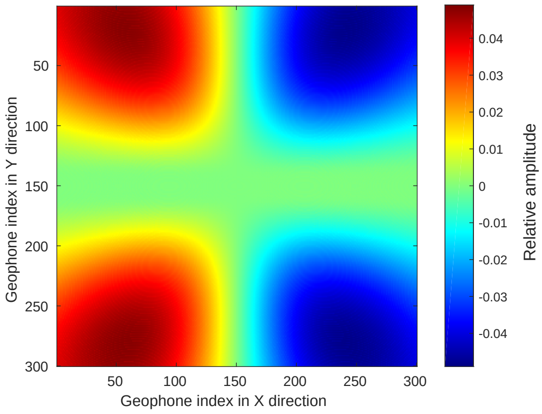

(a)

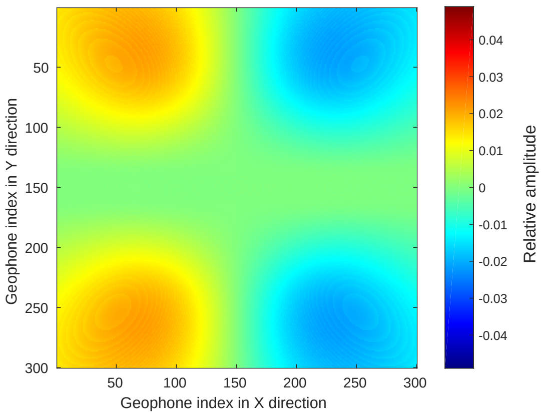

(b)

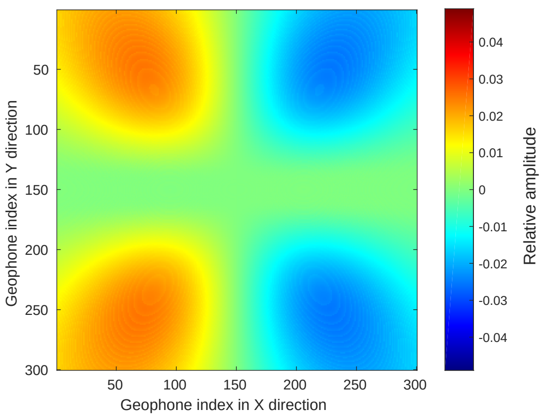

(c)

Fig. 19 Peak amplitudes of the direct P-wave in the (a) isotropic, (b) VTI and (c) HTI models for the surface array

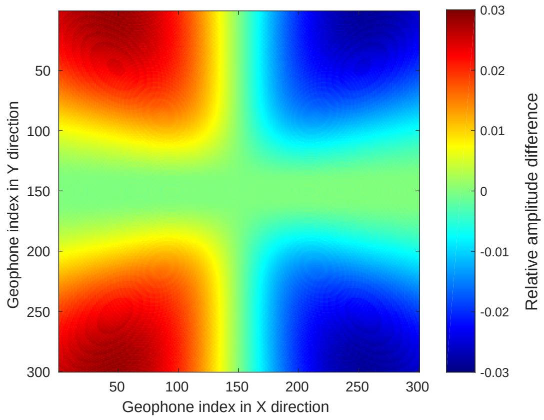

(a)

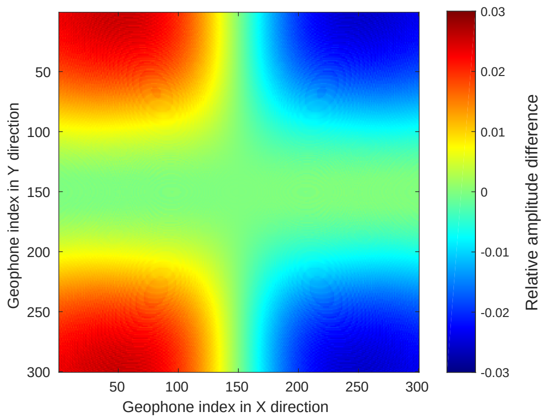

(b)

Fig. 20 Peak amplitude differences of the direct P-wave with respect to the isotropic case. (a) VTI model; (b) HTI model

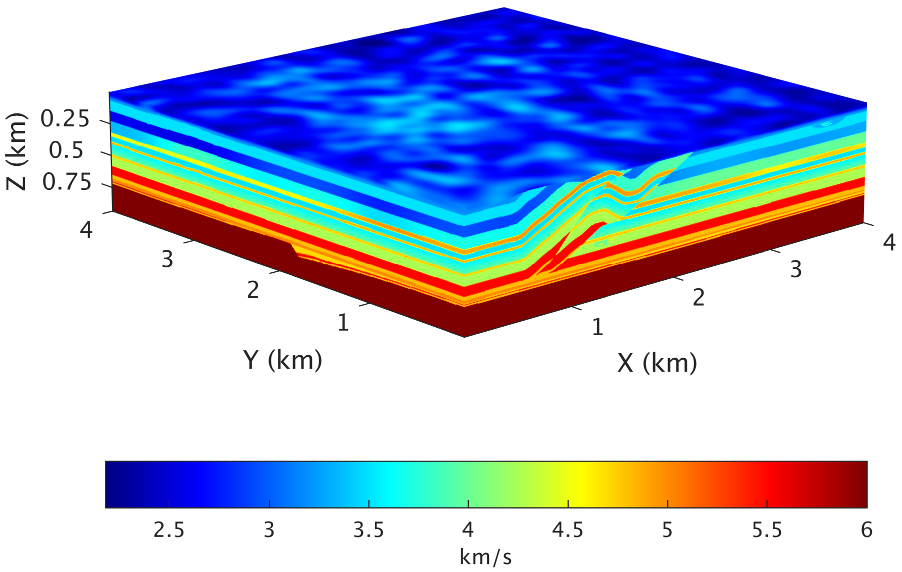

Fig. 21 P-wave velocity of the 3D overthrust model

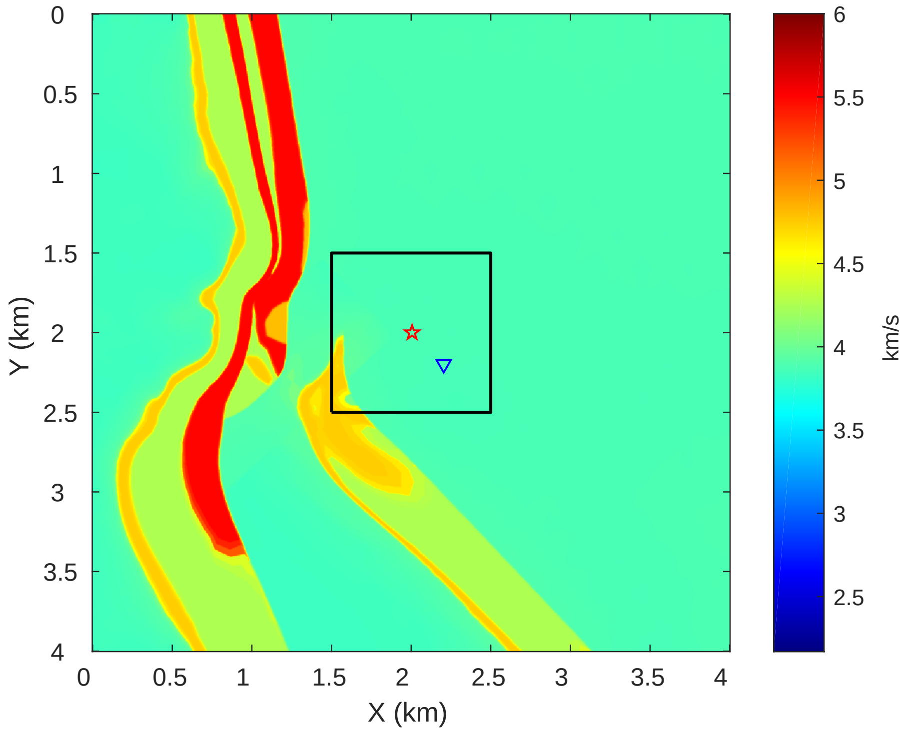

(a)

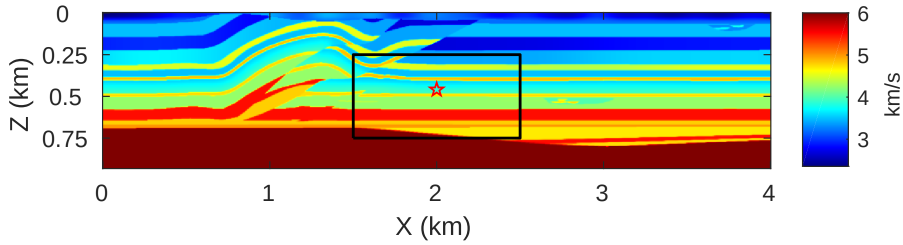

(b)

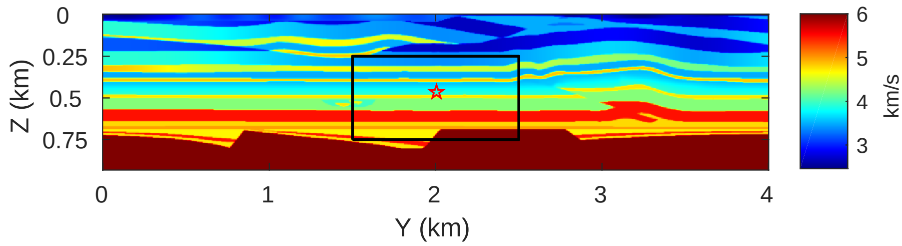

(c)

Fig. 22 Shown are P-wave velocity profiles of the 3D overthrust model. The red star represents source position; the black line exhibits the anisotropic region in the model; the blue triangle represents the horizontal projection of the vertical downhole array. (a) Velocity profile at the depth of microseismic source (0.46 km). (b) Velocity profile at 2 km in the Y direction. (c) Velocity profile at 2 km in the X direction

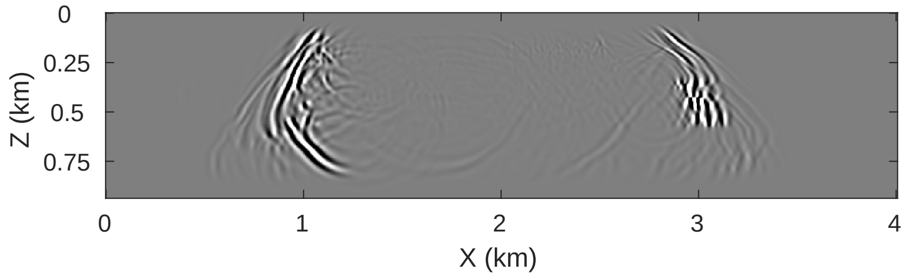

(a)

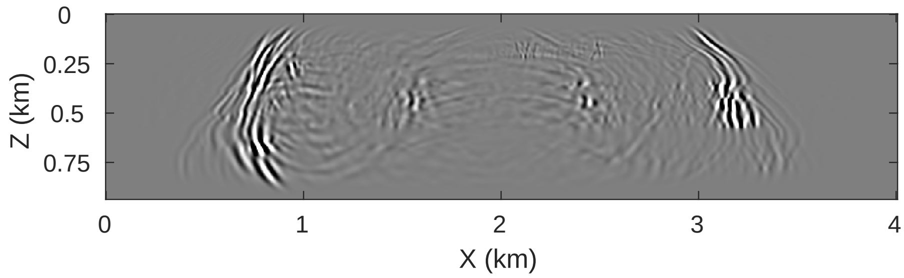

(b)

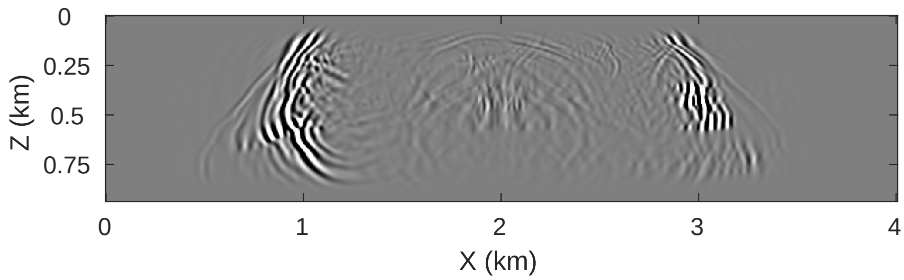

(c)

Fig. 23 Wavefield snapshots of velocity component in Y direction at 0.49 s and y=2 km. (a) Isotropic case. (b) VTI case. (c) HTI case

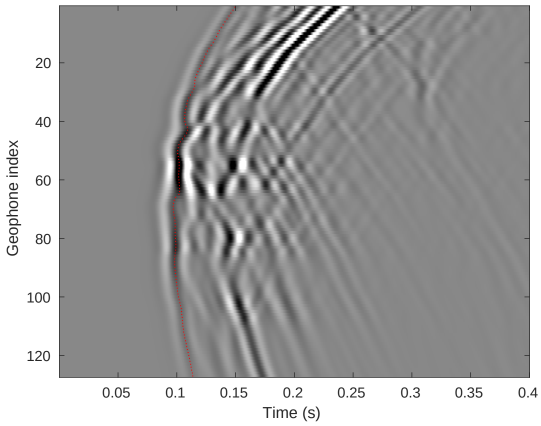

(a)

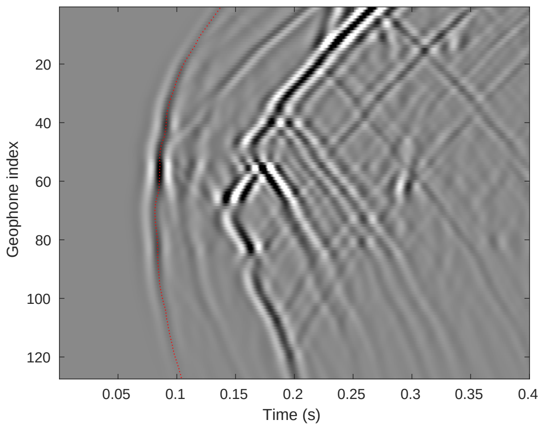

(b)

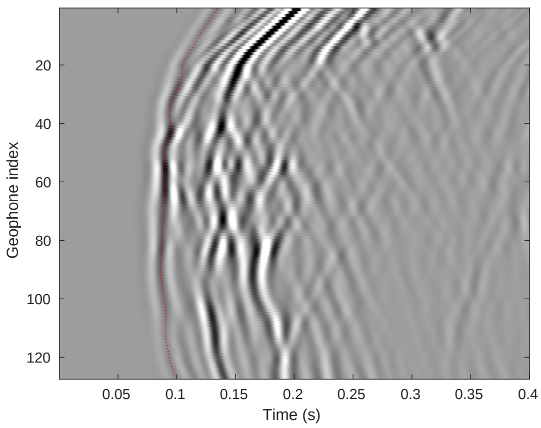

(c)

Fig. 24 The recorded seismograms in the downhole array for the (a) isotropic, (b) VTI and (c) HTI model. Red dotted lines represent the automatically picked direct P-wave wavefronts

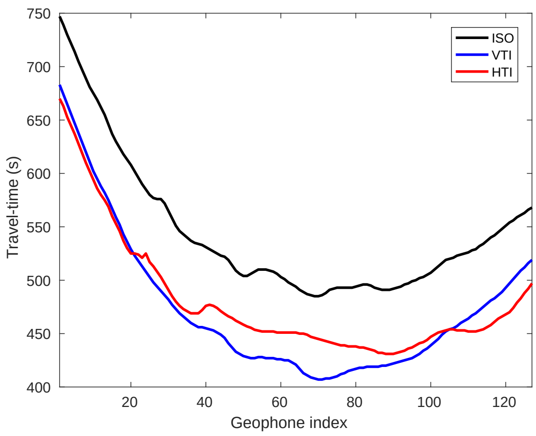

(a)

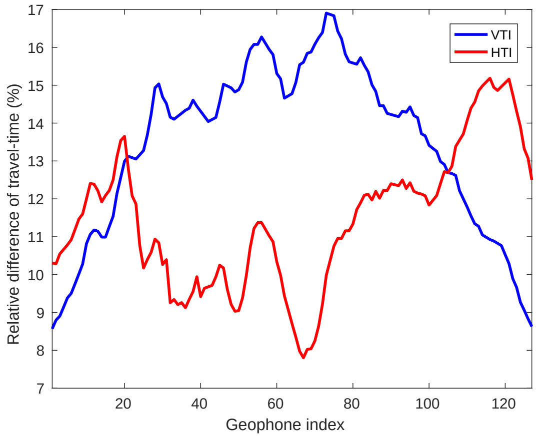

(b)

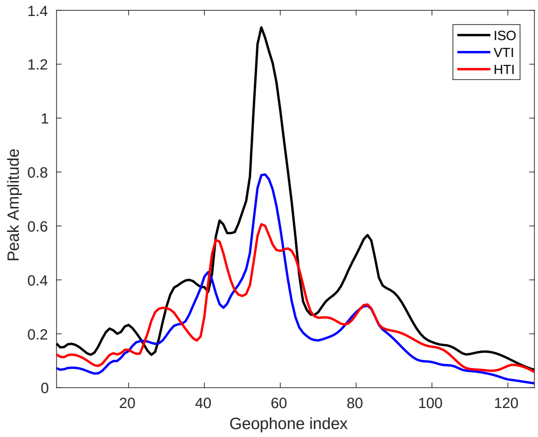

(c)

Fig. 25 Comparisons of travel-times and peak amplitudes of the direct P-wave for the isotropic, VTI and HTI model. Dark solid line represents value in the isotropic model; blue solid line represents value in the VTI model; red solid line represents value in the HTI model. (a) Travel-times of the direct P-wave. (b) Relative travel-time differences of the VTI and HTI model with respect to the isotropic model. (c) Peak amplitudes of the direct P-wave

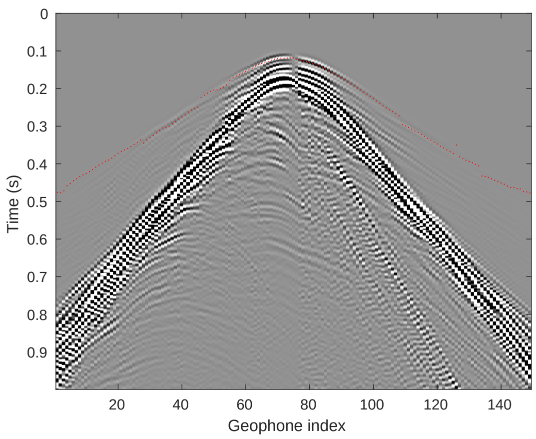

(a)

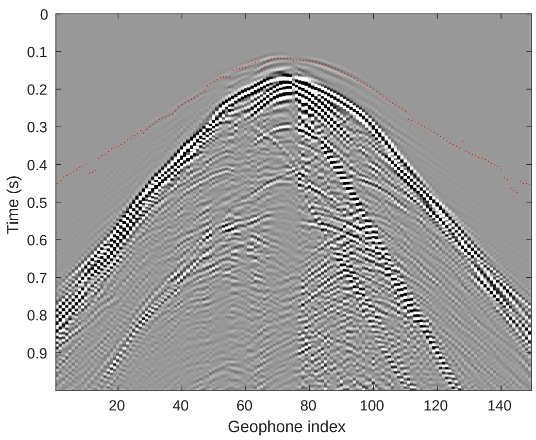

(b)

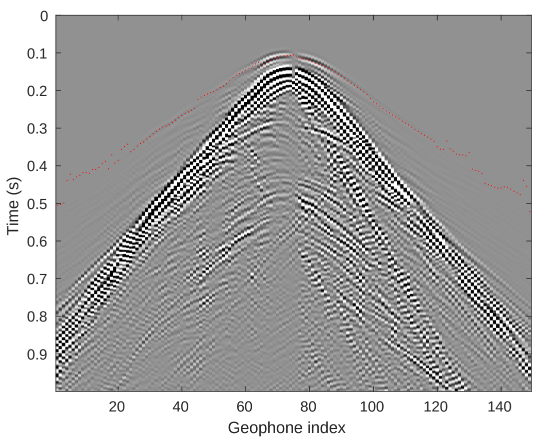

(c)

Fig. 26 The recorded seismic profiles in the surface array for the (a) isotropic, (b) VTI and (c) HTI model at the 70th receiver line in Y direction. Red dotted lines represent the automatically picked direct P-wave wavefronts

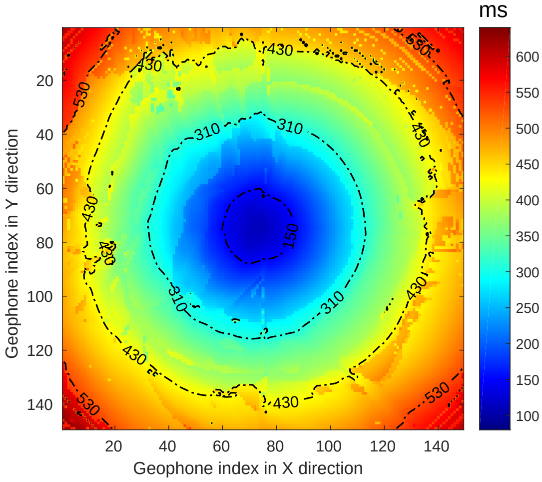

(a)

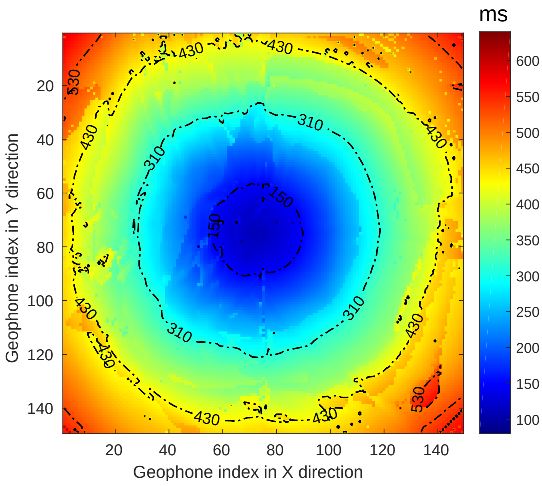

(b)

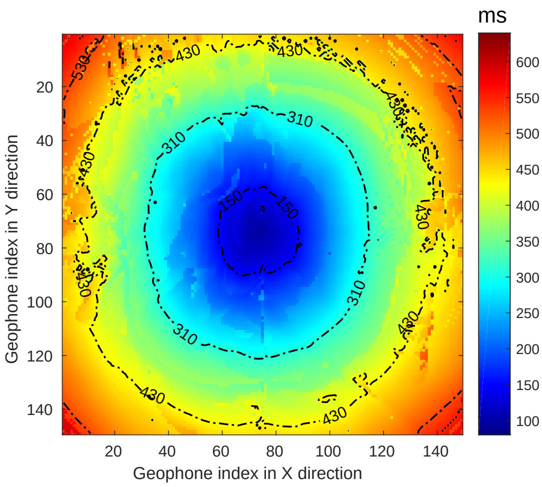

(c)

Fig. 27 Travel-times of the direct P-wave in the (a) isotropic, (b) VTI and (c) HTI model for the surface array. The contour lines of travel-times are also displayed in the figure. The unit of time in these figures is millisecond

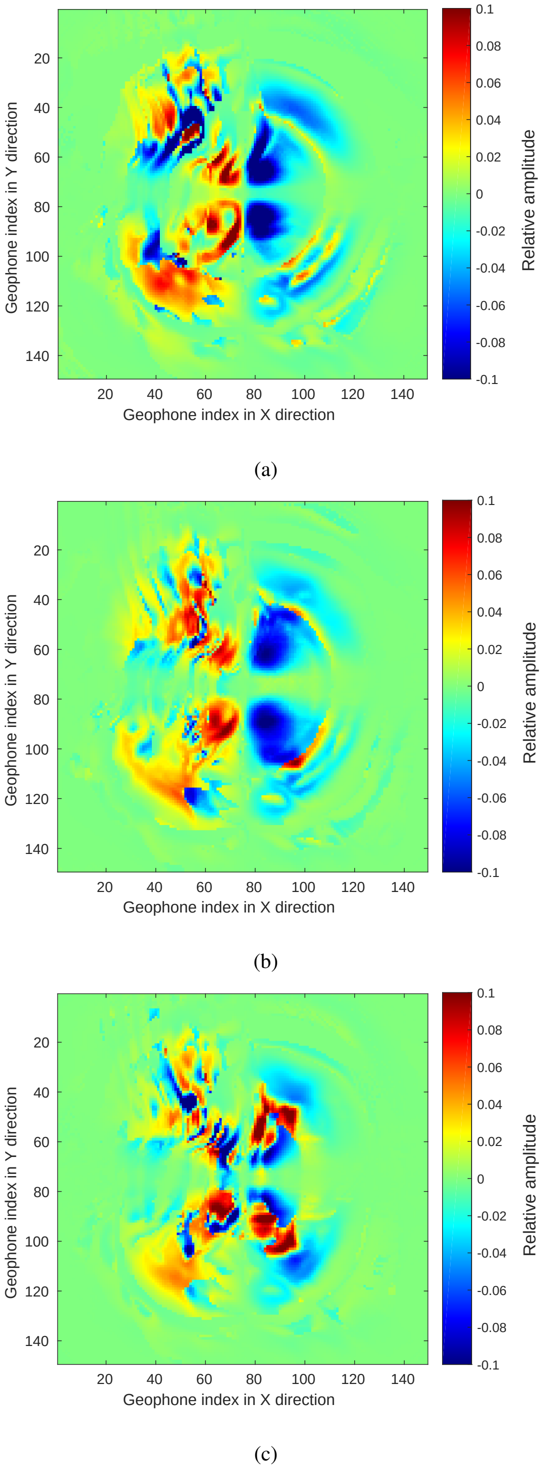

Fig. 28 Peak amplitudes of the direct P-wave in the (a) isotropic, (b) VTI and (c) HTI model for the surface array

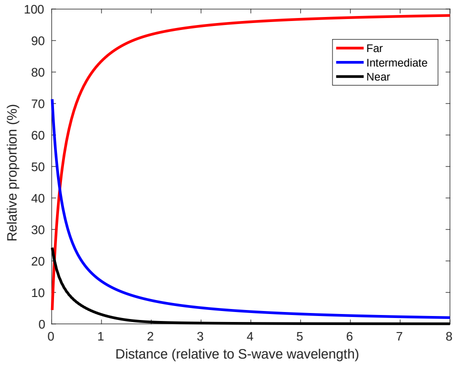

(a)

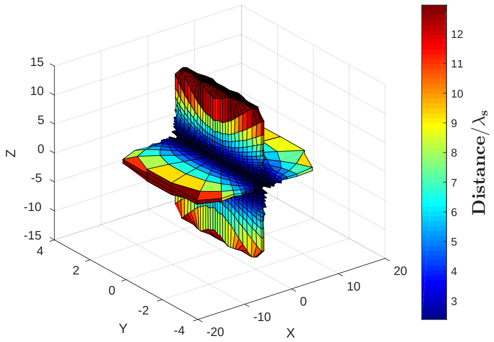

(b)

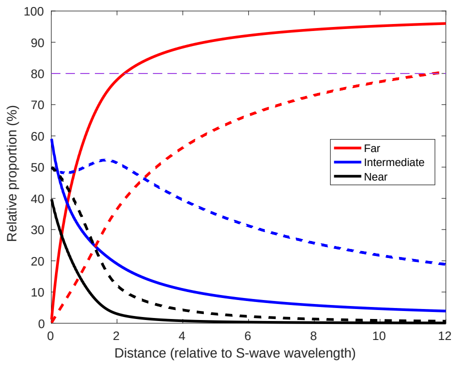

(c)

Fig. 29 (a) Relative magnitude of peak amplitude of the proportional part for near-field term, intermediate-field terms and far-field terms under certain parameters. (b) 3D map which shows the far-field distance in terms of S-wave wavelength in different directions for a 45° dip-slip double-couple source. Beyond this far-filed distance, the far-field terms will occupy more than 80% energy in the whole wavefield. (c) Relative magnitude of wavefields for near-field term, intermediate-field S-wave term and far-field S-wave term for a double-couple source in different directions. The solid lines show the scenario in direction which has a zenith angle of 45° and azimuth angle of 0°. The dashed lines show the scenario in direction which has a zenith angle of 5° and azimuth angle of 0°